MITIGATING DISTRIBUTION SHIFT IN MACHINE LEARNING-AUGMENTED HYBRID SIMULATION

JIAXI ZHAO* AND QIANXIAO LI[†]

Abstract.

We study the problem of distribution shift generally arising in machine-learning augmented hybrid simulation, where parts of simulation algorithms are replaced by data-driven surrogates. A mathematical framework is established to understand the structure of machine-learning augmented hybrid simulation problems and the cause and effect of the associated distribution shift. We show correlations between distribution shift and simulation error both numerically and theoretically. Then, we propose a simple methodology based on tangent-space regularized estimator to control the distribution shift, thereby improving the long-term accuracy of the simulation results. In the linear dynamics case, we provide a thorough theoretical analysis to quantify the effectiveness of the proposed method. Moreover, we conduct several numerical experiments, including simulating a partially known reaction-diffusion equation and solving Navier-Stokes equations using the projection method with a data-driven pressure solver. In all cases, we observe marked improvements in simulation accuracy under the proposed method, especially for systems with high degrees of distribution shift, such as those with relatively strong non-linear reaction mechanisms, or flows at large Reynolds numbers.

Key words. machine learning, distribution shift, regularization, error analysis, fluid dynamics

MSC codes. 68T99, 65M15, 37M05

1. Introduction. Many scientific computational applications, such as computational fluid dynamics (CFD) and molecular dynamics (MD) can be viewed as dynamical system modeling and simulation problems, which are tackled by rigorous numerical tools with theoretical guarantee [53]. However, in many cases a part of the simulation workflow, such as the Reynolds stresses in Reynolds-averaged Navier-Stokes equation (RANS) [1] and the exchange-correlation energies in density function theory used to compute force fields that drive MD simulations [30], depends on models that are either expensive to compute or even unknown in practice. One thus often resorts to a hybrid simulation method, where the known, resolved components of the dynamics are computed exactly, while the unresolved components are replaced by approximate, but computationally tractable models. For example, solving Navier-Stokes equations using the projection method involves two steps. In the first step, all the terms except for the gradient of the pressure are used to evolve the velocity. This step is computationally cheap and thus understood as the resolved part. Next, the pressure is solved from a Poisson equation and then used to correct the velocity. Most of the computational cost is contained in solving this Poisson equation, and we thereby viewed this as the unresolved part. We call such scientific computing problems with both resolved and unresolved parts "hybrid simulation problems". Similar problems are surveyed in [59] under the name of "Hybrid physics-DL models".

As machine learning becomes increasingly powerful in areas like computer vision and natural language processing, practitioners begin to use data-driven modules to model the unresolved part to carry out the simulation. For example, in [57] the author replaced the numerical Poisson solver of the unresolved part with a convolutional neural network trained using a novel unsupervised learning framework. Then, this data-driven model is coupled with resolved models and provides fast and realistic

^{*}Department of Mathematics, National University of Singapore, 117543, Singapore (ji-axi.zhao@u.nus.edu).

[†]Department of Mathematics & Institute for Functional Intelligent Materials, National University of Singapore, 117543, Singapore (qianxiao@nus.edu.sg).

2

simulation results in 2D and 3D. Similar ideas are used elsewhere, e.g. RANS [31] and LES [50]. We hereafter refer to this simulation procedure as machine-learning augmented hybrid simulation (MLHS). This structure represents a great part of the scientific machine learning research [62, 54] and will be the focus of this paper. In MLHS, a common problem appears: while the data-drive model performs well on the training data, the performance quickly deteriorates when iteratively applying it in simulation, driving the dynamics to some regimes that are not observed from the training source. Empirical evidences have been observed in various applications, such as CFD [50, 54, 39, 62], molecular dynamics [64, 63, 29], and iterative numerical solver [2], but these problems are not well-studied algorithmically and theoretically in the literature.

This issue has strong connections with the so-called distribution shift (DS) in computer science applications, especially in reinforcement learning and computer vision. Researchers use DS to refer to problems where training and testing distribution differ significantly. An example is an image classifier trained with images taken in the daytime that is tested under night conditions [25]. Therefore, the accuracy during the training itself cannot guarantee the performance during inference. To resolve this, researchers have systematically developed several methods, e.g. domain adaptation [10], ensemble learning [7], and meta-learning [58]. However, there are key differences between the distribution shift phenomena in MLHS and that in traditional applications between the DS phenomena in MLHS and computer vision. While distribution shift in computer vision lacks a theoretical model to describe [25], that in MLHS comes from dynamical systems for which we have abundant knowledge on the resolved parts of the models. For example, let us consider using the projection method [8] to solve the incompressible Navier-Stokes equation. Suppose we replace the Poisson pressure solver with a data-driven model based on neural networks. Then, the dynamics of this data-driven hybrid numerical solver will largely depend on the properties of the resolved numerical part of the projection method, which is well-studied [8]. By analyzing the stability properties of the dynamics, one can quantify which family of distribution shifts may arise and resolve them according to the information of the dynamics. Therefore, one can pose the following question: Can we use the information of resolved parts to design robust learning algorithms for unresolved parts to improve hubrid simulation?

In this paper, we first develop a mathematical framework to understand the origin of distribution shift in MLHS and how it may lead to simulation performance deterioration. We emphasize the difference between this instability issue in data-driven scientific computing and distribution shift in the machine learning literature, such as reinforcement learning and computer vision. Then, we propose an algorithm to improve the simulation accuracy by mitigating distribution shifts. We assume by manifold hypothesis [37] that the correct trajectories lie on a low-dimensional manifold of the high-dimensional space, e.g. the fluid configuration of the Navier-Stokes equation lies on the solution manifold of the high-dimensional grid space. The key idea is to combine the physical information of the resolved part of the model, i.e. Navier-Stokes equation and this manifold structure learned from the data to form a regularization term for the data-driven model. Intuitively speaking, this regularizer stabilizes the dynamics by preventing it from moving further away from the data manifold. Such movements may result in configurations that are either non-physical, or corresponds to different initial/boundary conditions. Therefore, preventing such movements reduces the severity of distribution shift, and the data-driven model will stay relatively accurate during the simulation, which promotes high simulation fidelity

in a long time interval. In implementation, we first use an autoencoder (AE) to parameterize the underlying data manifold. After this preprocessing, the AE is combined with the resolved dynamics and plugged into the loss function of the model as a regularization, which prevents the simulation from moving to unseen regimes. One then back-propagates this modified loss function to optimize the data-driven model. The algorithm is tested on several representative numerical examples to demonstrate its effectiveness. We show that the proposed approach can improve simulation accuracy under different extents of distribution shift. Indeed, the improvements become more significant in scenarios where the fidelity of the simulation is highly sensitive to errors introduced in the data-driven surrogates, such as transport-dominant fluid simulations and reaction-diffusion equations with relatively strong non-linear reactions. Specifically, in fluid simulations, naive data-driven surrogate models may quickly cause error blow-ups, but our method can maintain simulation accuracy over large time intervals.

The paper is structured as follows. In section 2, we establish a precise framework to identify the origins of distribution shift in MLHS. In section 3, we introduce our regularized learning algorithm motivated by the analysis of the previously identified form of distribution shift and theoretically understand its performance in the linear setting. We also discuss connections with the literature on control and system identification. In section 4, we validate our algorithm on several practical numerical cases, including simulating a reaction-diffusion equation and the incompressible Navier-Stokes equation.

- 2. Mathematical formulation of MLHS and the problem of distribution shift. In this section, we provide the mathematical formulation of MLHS and then identify the problem of distribution shift. In the first subsection, we give a general treatment, and we provide concrete examples in subsection 2.2.
- 2.1. The resolved and unresolved components in hybrid simulations. Throughout this paper, we consider the dynamics

(2.1)
$$\partial_t \mathbf{u} = \mathcal{L}(\mathbf{u}, \mathbf{y}, t), \quad \mathbf{y} = \phi(\mathbf{u}, t),$$

where \mathbf{u} is the resolved state variable, e.g. fluid velocity field or chemical concentration field. The vector \mathbf{y} is the unresolved variable that drives the dynamics for \mathbf{u} but is either expensive to compute or cannot be directly observed. Throughout the paper, we will omit writing the explicit time-dependence by using \mathbf{u} (\mathbf{y}) to denote $\mathbf{u}(t)$ ($\mathbf{y}(t)$) whenever there is no ambiguity. In numerical simulation, one always discretizes the ODE or PDE to obtain a finite-dimensional system, i.e. $\mathbf{u} \in \mathbb{R}^m, \mathbf{y} \in \mathbb{R}^n, \mathcal{L} : \mathbb{R}^m \times \mathbb{R}^n \times \mathbb{R}^n \times \mathbb{R}^n \times \mathbb{R}^n \times \mathbb{R}^n \times \mathbb{R}^n$. Therefore, we restrict the discussion to the finite dimension case where both \mathcal{L}, ϕ becomes mapping between finite-dimensional spaces, but most of the analysis here applies to the more general case of \mathbf{u}, \mathbf{y} belonging to an infinite dimensional Hilbert space. We adopt the following assumptions associated with (2.1):

- 1. Resolved component: \mathcal{L} is known, possibly non-linear.
- 2. Unresolved component: ϕ is either unknown or expensive to evaluate.

Given such a system, the goal is to first obtain information on the unresolved model and then integrate it with the resolved part to simulate the whole dynamics. This hybrid structure, which we call hybrid simulation problems, is general enough to include many applications, e.g. when simulating the trajectories of molecular dynamics which satisfy some stochastic differential equations or the time-evolution of fluid velocity fields following the Navier-Stokes equation. We focus on MLHS, a particular

variation of such hybrid simulation problems where the unresolved component is tackled by a data-driven method. This point will be made more precise in subsection 2.3. To simplify the analysis, we adopt the forward Euler time discretization for simulation

(2.2)
$$\widehat{\mathbf{u}}_{k+1} = \widehat{\mathbf{u}}_k + L(\widehat{\mathbf{u}}_k, \widehat{\mathbf{y}}_k) \Delta t, \qquad \widehat{\mathbf{y}}_k = \phi(\widehat{\mathbf{u}}_k),$$

while other consistent discretizations may be analyzed in the same spirit. Here we drop the dependence of L, ϕ on t to consider autonomous systems while our later discussion and algorithm are also applicable to non-autonomous systems.

2.2. Examples of hybrid simulation problems. Before moving on to distribution shift, we first provide some examples in MLHS of our interest, which are also closely related to our numerical experiments. We will present these examples according to the structure (2.1).

The first example is solving the 2D incompressible Navier-Stokes equation using the projection method [17, 8], a variant of which is as follows:

(2.3)
$$\frac{\partial \mathbf{u}}{\partial t} + (\mathbf{u} \cdot \nabla)\mathbf{u} - \nu \Delta \mathbf{u} = \nabla p, \quad \nabla \cdot \mathbf{u} = 0, \quad T \in [0, 1],$$

where $\mathbf{u} = (u(x, y, t), v(x, y, t))^T \in \mathbb{R}^2$ is the velocity and p is the pressure. Fix a regular grid size for discretization. The projection method can be written as follows

(2.4)
$$\mathbf{u}_{k+1} = \mathbf{u}_k + L(\mathbf{u}_k, p_k) \Delta t = \mathbf{u}_k + (\nu \Delta \mathbf{u}_k - (\mathbf{u}_k \cdot \nabla) \mathbf{u}_k - \nabla p_k) \Delta t, \\ p_k = \phi(\mathbf{u}_k) = \Delta^{-1} (\nabla \cdot (\nu \Delta \mathbf{u}_k - (\mathbf{u}_k \cdot \nabla) \mathbf{u}_k)),$$

We write Δ^{-1} as the formal inverse operator for the Laplace operator. The resolved part is performed by first stepping the convection and diffusion term then using pressure to correct the step, and the unresolved part is a Poisson equation that relates the unsolved state p_k with the velocity \mathbf{u}_k . Here, p_k represents the unresolved variable \mathbf{y}_k in our formulation (2.1).

In this method, the most expensive step is the pressure computation, which requires repeated solutions of similar large-scale linear equations. State-of-the-art solvers such as multigrid [5] and conjugate gradient [51] become prohibitively expensive when the problem size is large. Recently, a promising direction is replacing the Poisson solver by data-driven surrogate models. Ref. [57] replaces the pressure calculation step with a convolutional neural network trained with unsupervised learning by requiring the updated velocity to have zero divergence. In the same spirit, machine learning models such as tensor-based neural networks are used in [31] to replace classical turbulence modeling for unclosed Reynolds stress tensors. This model is then plugged into the Reynolds-averaged Navier-Stokes simulation to predict the flow separation. More recently, [41] combines the idea of reduced-order modeling with graph convolutional neural network to encode the reduced manifold and enable fast evaluations of parameterized PDEs.

The second example concerns simulations on two grids of different sizes. Let us continue with the projection method setting (2.4). Denote the time-evolution operator on grid size n as $f_n : \mathbf{u}_k^n \to \mathbf{u}_{k+1}^n$, which becomes very expensive to compute when n is large. Therefore, one may wish to replace the fine-grid solver with a coarse-grid one and add some corrections. This again reduces the computational burden for high-fidelity simulations. This structure shows up in various scientific computing situations, such as multigrid solvers [5], Reynolds-averaged Navier-Stokes (RANS) [42, 1], and large eddy simulation (LES) [67]. Suppose we have a fine grid with size $2n \times 2n$ and

a coarse grid with size $n \times n$, we use superscript n, 2n to denote the field defined on these two grids, i.e. $\mathbf{u}_k^n, \mathbf{u}_k^{2n}$. Moreover, we fix an interpolation and a restriction operator between fields on these two grids:

$$(2.5) I_n^{2n}: \mathbb{R}^{n \times n} \to \mathbb{R}^{2n \times 2n}, \quad R_{2n}^n: \mathbb{R}^{2n \times 2n} \to \mathbb{R}^{n \times n}.$$

Now, we can state the second hybrid simulation problem as follows:

(2.6)
$$\begin{cases} \mathbf{u}_{k+1}^{2n} = I_n^{2n} \circ f_n(R_{2n}^n(\mathbf{u}_k^{2n})) + \mathbf{y}_k^{2n}, \\ \mathbf{y}_k^{2n} = \phi(\mathbf{u}_k^{2n}). \end{cases}$$

In detail, the resolved component contains a solver of the evolution equation over the coarse grid which marches forward by one time step, with the field given by a restriction of the field on the fine grid. Then, the next step field configuration is interpolated to the fine grid and the unresolved component serves to correct the deviation of the field variables between simulating on grids of different sizes. The unresolved variables \mathbf{y}_k^{2n} can be calculated if we have accurate simulation results \mathbf{u}_k^{2n} on the fine grid by $\mathbf{y}_k^{2n} = \mathbf{u}_{k+1}^{2n} - I_n^{2n} \circ f_n(R_{2n}^n(\mathbf{u}_k^{2n}))$. In the literature, [22] treats the smoothing algorithm in multigrid solver as unresolved components and other procedures such as restriction and prolongation as resolved components. This fits into our framework of MLHS. They introduce a supervised loss function based on multigrid convergence theory to learn the optimal smoother and improve the convergence rate over anisotropic rotated Laplacian problems and variable coefficient diffusion problems. In [35], the authors apply neural networks with non-linear regression to fit key fluid features and sub-grid stresses. Going beyond this, [39] adds neural emulation to offline learning to prevent the trajectories from deviating away from the ground truth. This data-driven model is plugged into hybrid simulations to test its ability to preserve coherent structure and scaling laws.

2.3. Learning the unresolved model and distribution shift. We assume that the resolved part \mathcal{L} is known, or we at least have access to a gray box that can perform its evaluation and compute its gradients. While the unresolved part is unknown, we can access data tuples $\{(\mathbf{u}_1,\mathbf{y}_1,t_1),(\mathbf{u}_2,\mathbf{y}_2,t_2),\cdots,(\mathbf{u}_N,\mathbf{y}_N,t_N)\}$ which are obtained either by physical experiments or accurate but expensive numerical simulations. The goal is hence to construct an approximate mapping $(\mathbf{u}_k, t_k) \mapsto \mathbf{y}_k$ from this dataset. Viewing this as a supervised learning task, there are many existing methods based on empirical risk minimization [18, 19, 27]. One of the simplest methods is to minimize the mean squared error. Given a parameterized model ϕ_{θ} , e.g. a Gaussian process or a neural network, we learn from data the optimal value of the parameter θ that minimizes the error, i.e. $\widehat{\theta} = \arg\min_{\theta} \mathbb{E}_{(\mathbf{u}, \mathbf{y})} \|\mathbf{y} - \phi_{\theta}(\mathbf{u}, t)\|_{2}^{2}$. However, due to the dynamical structure, the i.i.d. assumption in statistical learning [19] no longer holds in MLHS. In particular, data belonging to the same dynamical trajectory will have a large correlation. Moreover, an appropriate performance evaluation is not necessarily the precise identification of the system [33] but the accuracy of the prediction of the trajectory over long times. This is also known as a priori and a posteriori performance in the closure modeling literature [48]. Therefore, it is reasonable to expect that simple empirical risk minimization (which many existing MLHS works employ [54, 45]) may not be the optimal method. We will demonstrate this by using the least squares estimator as a baseline comparison to our approach in section 4.

After determining the parameters of the unresolved model, one can perform hybrid simulations to obtain new trajectories, i.e.

(2.7)
$$\widehat{\mathbf{u}}_{k+1} = \widehat{\mathbf{u}}_k + L(\widehat{\mathbf{u}}_k, \widehat{\mathbf{y}}_k, t_k) \Delta t, \quad \widehat{\mathbf{y}}_k = \phi_{\widehat{\theta}}(\widehat{\mathbf{u}}_k, t_k).$$

Notice we add hat superscript to all the quantities related to this simulated dynamics to distinguish them from the ground truth $(\mathbf{u}_k, \mathbf{y}_k)$. We measure the performance of the simulator by the error along the whole trajectory, i.e.

(2.8)
$$\min \sum_{k=1}^{n} \|\mathbf{u}_{k} - \widehat{\mathbf{u}}_{k}\|_{2}^{2},$$

where \mathbf{u}_k s belongs to the true trajectory and $\hat{\mathbf{u}}_k$ s the simulated one with the same initial condition.

We begin by illustrating the issue of distribution shift by analyzing the trajectory error. For simplicity of presentation, we assume that the model hypothesis space $\{\phi_{\theta}: \theta \in \Theta\}$ is bias-free, meaning that there exists $\theta^* \in \Theta$ such that $\phi = \phi_{\theta^*}$. In the general case where the hypothesis space is universal but not closed, this equality would be replaced by an approximate one, but the argument follows analogously. Comparing (2.1) and (2.7), we have

(2.9)
$$\widehat{\mathbf{u}}_{k+1} - \mathbf{u}_{k+1} = \widehat{\mathbf{u}}_k - \mathbf{u}_k + \left(L(\mathbf{u}_k, \phi_{\widehat{\theta}}(\mathbf{u}_k)) - L(\mathbf{u}_k, \phi_{\theta_*}(\mathbf{u}_k)) \right) \Delta t + \left(L(\widehat{\mathbf{u}}_k, \phi_{\widehat{\theta}}(\widehat{\mathbf{u}}_k)) - L(\mathbf{u}_k, \phi_{\widehat{\theta}}(\mathbf{u}_k)) \right) \Delta t.$$

The error introduced by moving one step forward is thus decomposed into two parts: the error associated with the estimator $\hat{\theta}$: $L(\mathbf{u}_k, \phi_{\hat{\theta}}(\mathbf{u}_k)) - L(\mathbf{u}_k, \phi_{\theta_*}(\mathbf{u}_k))$, and the other error $L(\widehat{\mathbf{u}}_k, \phi_{\widehat{\boldsymbol{\theta}}}(\widehat{\mathbf{u}}_k)) - L(\mathbf{u}_k, \phi_{\widehat{\boldsymbol{\theta}}}(\mathbf{u}_k))$. The former resembles the error appearing in classical statistical inference problem under the i.i.d. setting since \mathbf{u}_k follows an identical distribution of the training dataset. While the latter is different in the sense that $\hat{\mathbf{u}}_k$ and \mathbf{u}_k may come from distributions of their respective driving dynamics, which are different since $\theta_* \neq \widehat{\theta}$ due to noisy labels, few data points, or having an under-determined system. The difference between MLHS and statistical learning is also emphasized in [59]. The latter error $L(\widehat{\mathbf{u}}_k, \phi_{\widehat{\theta}}(\widehat{\mathbf{u}}_k)) - L(\mathbf{u}_k, \phi_{\widehat{\theta}}(\mathbf{u}_k))$ is rather akin to the issue of stability in numerical partial differential equations: although the error in each step is relatively small, it can accumulate exponentially as time step iterates, driving $\hat{\mathbf{u}}_k$ to completely different regimes where we have not observed in the data $\mathbf{u}_k, k = 1, \cdots, N$. As a result, the data-driven model ϕ can no longer be trusted to be accurate, since it is trained on data from a different distribution. This may then lead to a vicious cycle, where further deterioration of trajectory error occurs, leading to an increasing discrepancy between the distributions. Consequently, one can understand the distribution shift as a large discrepancy between the true distribution ρ of \mathbf{u}_k and simulated distribution $\widehat{\rho}$ of $\widehat{\mathbf{u}}_k$. Concretely, we adopt the following definition for a simulation algorithm (2.7) to have distribution shift:

(2.10)
$$\limsup_{t \to \infty} \frac{\log d(\rho_t, \widehat{\rho}_t)}{t} \ge c > 0,$$

where ρ_t , $\hat{\rho}_t$ denote the distributions of the ground truth $\mathbf{u}(t)$ and the simulation $\hat{\mathbf{u}}(t)$ starting from the initial condition with same distribution ρ_0 . $d(\cdot, \cdot)$ is an appropriate distance between probability distributions. We emphasize that the definition of the distribution shift relates to the time because of the dynamic nature of the problem, which is different from traditional machine learning settings [25]. The problem of distribution shift occurs commonly in MLHS. For example, [31, 61, 43] all observe unphysical solutions when substituting Reynolds stresses models learned from direct numerical simulation database into RANS. Ref. [61] attributes this to the ill-conditioning of the RANS problems and propose a method to treat Reynolds stresses

implicitly. References [50, 49] deal with the subgrid-scale modeling in LES simulations by using neural networks. Improved performance in simulations is achieved by taking into consideration the whole trajectory accuracy in the loss function, which implicitly combats distribution shift. Despite several empirical successes, a general theoretical framework to understand and combat distribution shift in MLHS is lacking. The current paper aims to make progress in this direction.

Let us illustrate the problem of distribution shift using numerical examples. We solve the 2D FitzHugh-Nagumo reaction-diffusion equation over a periodic domain $[0, 6.4] \times [0, 6.4]$, whose dynamic is given by

(2.11)
$$\frac{\partial \mathbf{u}}{\partial t} = D\Delta \mathbf{u} + \phi(\mathbf{u}), \quad T \in [0, 20],$$

$$\phi(\mathbf{u}) = \phi(u, v) = \begin{pmatrix} u - u^3 - v + \alpha \\ \beta(u - v) \end{pmatrix},$$

where $\mathbf{u} = (u(x, y, t), v(x, y, t))^T \in \mathbb{R}^2$ are two interactive components, D is the diffusion matrix, and $\phi(\mathbf{u})$ is source term for the reaction. We fix the parameters to $\alpha = 0.01, \beta = 1.0, D = \begin{pmatrix} 0.05 & 0 \\ 0 & 0.1 \end{pmatrix}$, where the system is known to form Turing patterns [36]. Assuming that we do not know the exact form of the reaction term $\phi(\mathbf{u})$, the resolved part is the diffusion term and the unresolved part is the non-linear reaction term. The ground truth data is calculated using the semi-implicit Crank-Nicolson scheme with fully explicit discretization for the non-linear term. Assuming we do not know that the reaction term is pointwise in space, we use a convolutional neural network-based model to learn it based on ordinary least squares (OLS). Specifically, we solve the least squares problem $\min_{\theta} \mathbb{E}_{\mathbf{u}} \|\phi_{\theta}(\mathbf{u}) - \phi(\mathbf{u})\|_{2}^{2}$ using Adam [24]. Moreover, we conduct an ablation study where the unresolved model consists of the exact form of the non-linear term as in (2.11), plus a random Gaussian noise whose variance is set equal to the optimization error of the OLS estimator, which is 10^{-4} in the following experiments. By comparing this and the simulation based on the OLS model, we can identify the source of the accumulating trajectory error as either the estimation error of the unresolved model or the shift in the distribution of the input data fed to the unresolved model. More details on the data generation and optimization procedure is described in subsection 2.1 and 2.2 of supplementary materials. We simulate this PDE with a test initial condition sampled from the same distribution as training trajectories and compare the results with the ground truth. We present the comparison in Figure 1.

The first three rows display the snapshots of ground truth, simulated fields, and ablation study simulation at time steps: 0, 100, 200, 300, and 500. (d) plots the relative error (solid curve) and distribution shift (dotted curve) between two flow configurations at the corresponding time. The error is defined as $\frac{\|\widehat{\mathbf{u}}_t - \mathbf{u}_t\|_2}{\|\mathbf{u}_t\|_2}$ at each time step t instead of the whole trajectory as in (2.8). The plotted distribution shift roughly measures the average discrepancy between the distributions of \mathbf{u}_k and $\widehat{\mathbf{u}}_k$ at time step k, and is calculated using an autoencoder explained in subsection 3.2. As can be observed, it does not take a very long time for the distribution shift issue to be severe enough using the OLS estimator. Comparing the OLS error and distribution shift with those of the ablation study, we conclude that the estimation error is not the main cause of the trajectory error, since the ablation-study trajectory has the same magnitude of estimation error, but has a much smaller trajectory error and distribution shift. Moreover, in both cases the relative error of the trajectory has the

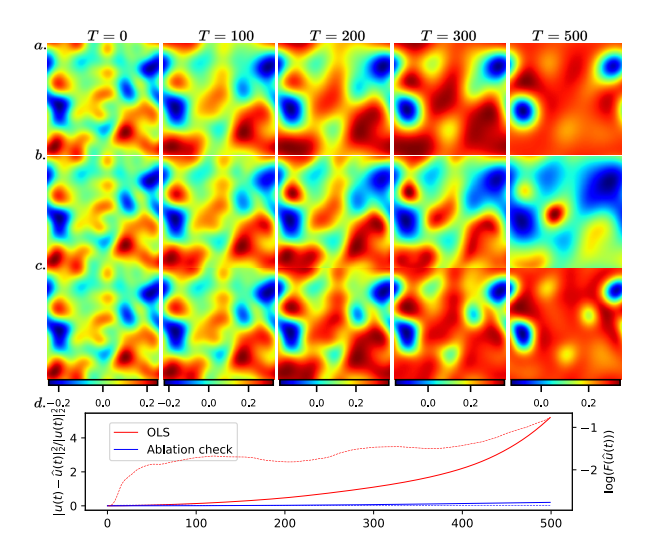


Fig. 1. The first three rows display the snapshots of ground truth, simulated fields, and ablation study simulation at time steps: 0, 100, 200, 300, and 500. (d) plots the relative error (solid line) and distribution shift (dash line) between two flow configurations at the corresponding time. The error is defined as $\frac{\|\widehat{\mathbf{u}}_t - \mathbf{u}_t\|_2}{\|\mathbf{u}_t\|_2}$ at each time step t instead of the whole trajectory as in (2.8). The plotted distribution shift roughly measures the average discrepancy between the distributions of \mathbf{u}_k and $\widehat{\mathbf{u}}_k$ at time step k, and is calculated using an autoencoder explained in subsection 3.2. Although the OLS estimator and ablation-study estimator share the same error magnitude for unresolved models, their long-time trajectory performance forms sharp contrasts, indicating the optimization error of the unresolved model could not explain the failure in long-time trajectory prediction.

same trend as the distribution shift, indicating correlations.

Indeed, this phenomenon is ubiquitous in modern MLHS [59, 64, 54]. As a second example, we solve the Navier-Stokes equation (2.3) using projection method (2.4) where the pressure solver is replaced by a learned convolutional neural network predictor. The predictor is optimized over data pairs of fluid velocity and pressure obtained from high-fidelity simulation to attain an error of 10^{-5} . Due to the complexity of the projection solver and grid issue, we do not conduct an ablation study in this case. The distribution shift in Figure 2 turns out to be more severe when we simulate the incompressible Navier-Stokes equation. After 160 time steps, the fluid configuration becomes rough and un-physical. Here, we again observe that the DS and error increase together, suggesting correlations. In the next section, we will make this connection precise, and develop principled methods to control the distribution shift, thereby improving the prediction fidelity.

- **3.** Theoretical analysis and algorithm. In this section, we first put the distribution shift issue into a theoretical framework. Then, we introduce and analyze our algorithm in this section. We will provide rigorous study of the linear case and use this to motivate the algorithm.
- 3.1. Distribution shift in linear dynamics and motivation of tangent-space regularized estimator. As there exist few tools to tackle the general non-linear dynamics (2.1), we switch to the simpler case of linear dynamics, which also capture some key features in general situations. We consider the following the hybrid

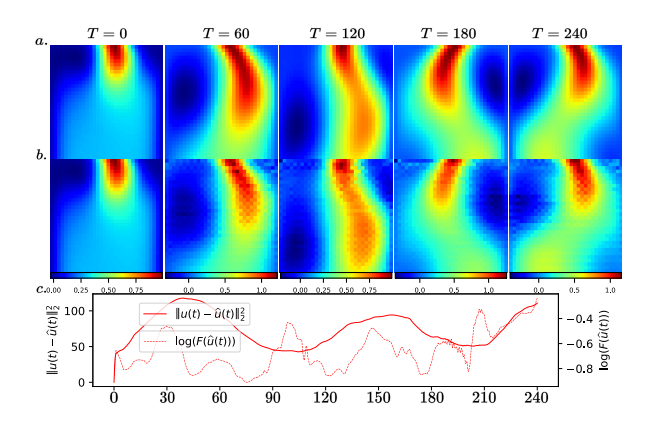


FIG. 2. Configurations of the Navier-Stokes equation simulation with Reynolds number 200 at time step: 0, 60, 120, 180, 240: (a) ground truth (b) simulated fluid field using OLS estimator. We only show the velocity field over part of the domain. The dynamic blows up in the last configuration, which does not show up in the case of reaction-diffusion equations. This can be explained by the fact that the Navier-Stokes equation is more unstable than reaction-diffusion equations. In (c), we illustrate the error along the trajectories, the distribution shift.

simulation problem

(3.1)
$$\frac{d\mathbf{u}}{dt} = A\mathbf{u} + B\mathbf{y}, \quad \mathbf{u} \in \mathbb{R}^m, \mathbf{y} \in \mathbb{R}^n, A \in \mathbb{R}^{m \times m}, B \in \mathbb{R}^{m \times n}$$
$$\mathbf{y} = C^*\mathbf{u}, \quad C^* \in \mathbb{R}^{n \times m}.$$

Such structures appear in many scenarios, e.g. finite difference solution of discretized linear PDEs and linear control problems. Alternatively, one can think of this linear system as the linearization of the non-linear dynamics (2.1) about some steady-state.

We assume that the state variables \mathbf{u}_i s in training data come from several trajectories and \mathbf{y}_i s may be subject to some random measurement error, i.e. $\mathbf{y}_i = C^*\mathbf{u}_i + \epsilon_i$, or in matrix form $Y = C^*\mathbf{U} + \epsilon$. The key point is that these trajectories may belong to a low-dimensional subspace in the high-dimensional state space. This is the case for many scientific computing problems, e.g. parametric elliptic PDE [3] and is also related to the notions of Kolmogorov N-width and the manifold hypothesis [11]. Although transport-dominated problems with low-decaying rates of the Kolmogorov N-width are difficult to approximate using linear reduced-order models, a large amount of literature [20, 21] show evidence of the existence of coherent structures in turbulence and their low-dimensional nature. Moreover, recent work [9] using nonlinear model reduction has achieved efficient reduction over this type of problems.

We use $V \subset \mathbb{R}^m$ to denote the subspace that contains all the training data \mathbf{u}_i . In this setting, the appearance of this low-dimensional structure may be caused by two different situations. In the first situation, the initial value of \mathbf{u} is supported on the subspace spanned by several eigenvectors of the evolution operator $e^{(A+BC^*)}$, i.e.

$$(3.2) \quad \mathbf{u}_0 \in \operatorname{span}\{\mathbf{v}_1, \mathbf{v}_2, \cdots, \mathbf{v}_l\}, \quad e^{(A+BC^*)}\mathbf{v}_1 = \operatorname{eig}_1\mathbf{v}_1, \cdots, e^{(A+BC^*)}\mathbf{v}_l = \operatorname{eig}_l\mathbf{v}_l,$$

Then, all the training data \mathbf{u}_i belong to this subspace, i.e. $V = \text{span}\{\mathbf{v}_1, \mathbf{v}_2, \dots, \mathbf{v}_l\}$. The second situation is that the dynamics is degenerate in the sense that the evolution matrix A is not of full rank. This will not appear in the differential formulation as infinitesimal transformations in the form $e^{(A+BC^*)\Delta t}$ are always non-degenerate.

However, for a discrete dynamic $\mathbf{u}_{k+1} = A\mathbf{u}_k + B\mathbf{y}_k$, $\mathbf{y}_k = C^*\mathbf{u}_k$, if the matrix $A + BC^*$ is degenerate, then all the data \mathbf{u}_k will belong to the range of this operator $A + BC^*$, which is a proper subspace. Most cases of scientific computing applications belong to the first class. Due to the degeneracy in the training data, the least squares solution is not unique. Hence, various empirical regularizations (e.g. ℓ^2 regularization) can be introduced to obtain an estimator with desirable properties.

Now, suppose one obtains an estimator \widehat{C} , one can calculate several error metrics. The first is the test error

(3.3)
$$l_{\text{OLS}}(\widehat{C}) = \mathbb{E} \left\| (\widehat{C} - C^*) \mathbf{u} \right\|_2^2,$$

where \mathbf{u} is sampled from the low dimensional subspace V and follows the same distribution as the training data. We refer to this as the statistical estimation error or a priori error. However, we are interested in the a posteriori error of the simulated dynamics

(3.4)
$$\frac{d\widehat{\mathbf{u}}}{dt} = A\widehat{\mathbf{u}} + B\widehat{\mathbf{y}}, \quad \widehat{\mathbf{y}} = \widehat{C}\widehat{\mathbf{u}},$$

compared to the ground truth ${\bf u}$ with the same initial condition. The time evolution of their difference is given by

(3.5)
$$\frac{d}{dt}(\widehat{\mathbf{u}} - \mathbf{u}) = (A + B\widehat{C})\widehat{\mathbf{u}} - (A + BC^*)\mathbf{u}$$
$$= (A + B\widehat{C}) P_V(\widehat{\mathbf{u}} - \mathbf{u}) + B(\widehat{C} - C^*)\mathbf{u} + (A + B\widehat{C})(\widehat{\mathbf{u}} - P_V\widehat{\mathbf{u}}),$$

where P_V is the orthogonal projection onto the data subspace V, and we have P_V $\mathbf{u} = \mathbf{u}$ since \mathbf{u} belongs to the data subspace. As derived in (3.5), the overall error of the trajectory during evolution can be decomposed into three parts. In the following, we make a detailed analysis of each term.

The first term can be viewed as an amplitude and stability factor of the error propagation of the simulated dynamics inside the data manifold V. If we assume the ground truth dynamics is stable in V, while not necessary to be stable over the whole state space, then this term can be simply bounded by the spectral information of the generator $(A + B\hat{C}) P_V$, see details in Proof 2.

The second term is simply the statistical estimation error of the estimator \widehat{C} defined in (3.3). Given that the initial condition \mathbf{u}_0 of the training and test trajectories are sampled from the same distribution, this term is well-bounded in classical statistical learning theory [19], provided the number of data tuples is sufficiently large. In particular, this error has nothing to do with the distribution shift.

Now we move to the last part $(A + B\hat{C})(\hat{\mathbf{u}} - P_V \hat{\mathbf{u}})$, which can be more easily understood from a geometric viewpoint. The last factor $(\hat{\mathbf{u}} - P_V \hat{\mathbf{u}})$ measures how far the simulated trajectory is away from the data subspace V, i.e. $\|\hat{\mathbf{u}} - P_V \hat{\mathbf{u}}\|_2 = \operatorname{dist}(\hat{\mathbf{u}}, V)$. In other words, this term measures how far the simulated trajectory's distribution "shifts" from the true distribution. This is exactly the term we want to control to maintain simulation fidelity. This term forms a sharp contrast with the two terms previously mentioned in the sense that it is not automatically bounded in most algorithms for estimating \hat{C} . We will illustrate this point further by deriving an error bound of the simulated dynamics, showing its sensitive dependency on the distribution shift term. Thus, we can improve a posteriori accuracy if we combat such distribution shifts.

Now, we can formally write the error propagation along the simulated dynamics as

$$(3.6) \quad \widehat{\mathbf{u}}(T) - \mathbf{u}(T) \\ = \int_0^T e^{(A+B\widehat{C}) \operatorname{P}_V(T-t)} \left(B(\widehat{C} - C^*) \mathbf{u}(t) + (A+B\widehat{C}) (\widehat{\mathbf{u}}(t) - \operatorname{P}_V \widehat{\mathbf{u}}(t)) \right) dt.$$

The exponential factor $e^{(A+B\widehat{C})P_V(T-t)}$ corresponds to the first term while two terms in the bracket that follows correspond to the second and the third terms mentioned above. The distribution shift term in MLHS, i.e. the second term in the bracket is far different from classical machine learning concepts such as covariate shift and label shift. In computer vision, the cause of distribution shift may be extrinsic [25], i.e. the pictures in training sets are all taken during the daytime while those for testing are all taken at night. Such shifts are hard to model, so their resolution tends to depend on data augmentation and related techniques, e.g. the Dagger algorithm [23, 47], where instead of changing the optimization problem, the data source is modified. This shares many similarities with adversarial training, which also adds more data to the training set to make the prediction robust under adversarial attack, a typical distribution shift in the area of computer vision [15]. In contrast, in our setting, the distribution shift is intrinsically driven by the hybrid simulation structure of which we have partial knowledge. Hence, we can quantify this distribution shift and design specific algorithms to mitigate them.

Returning to the linear problem, in order to guarantee that the error $\hat{\mathbf{u}} - \mathbf{u}$ is bounded over the simulated trajectory, a natural choice is to use a regularization for $\|\hat{\mathbf{u}} - \mathbf{P}_V \hat{\mathbf{u}}\|_2$. The most naive choice would be $\|\hat{\mathbf{u}} - \mathbf{P}_V \hat{\mathbf{u}}\|_2$ itself, but a problem is that $\hat{\mathbf{u}}$ is calculated via hybrid simulation until time t, which corresponds to a rather complicated computational graph. This makes subsequent gradient-based optimization computationally expensive. Hence, we take advantage of a one-step predictor, where we set $\hat{\mathbf{u}}_{k+1} = \mathbf{u}_k + (A\mathbf{u}_k + B\hat{C}\mathbf{u}_k)\Delta t$, meaning that $\hat{\mathbf{u}}_{k+1}$ is calculated based on a single step of the simulated dynamics from the ground truth solution \mathbf{u}_k . Assuming $\mathbf{u}_k \in V$, one has

(3.7)
$$\|\widehat{\mathbf{u}}_{k+1} - \mathbf{P}_V \widehat{\mathbf{u}}_{k+1}\|_2 = \Delta t \left\| \mathbf{P}_{V^{\perp}} (A\mathbf{u}_k + B\widehat{C}\mathbf{u}_k) \right\|_2,$$

and we may penalize the right-hand side to promote trajectory alignment with the data subspace. Wrapping up all the ingredients, we state the loss function in the linear case as

$$\min_{C} l(C) := \min_{C} \mathbb{E}_{(\mathbf{u}, \mathbf{y})} \left(\|\mathbf{y} - C\mathbf{u}\|_{2}^{2} + \lambda \|\mathbf{P}_{V^{\perp}}(A + BC)\mathbf{u}\|_{2}^{2} \right),$$

and here λ is a penalty strength parameter that can be chosen during training. We briefly discuss in subsection 2.5 of supplementary materials on choosing λ .

In the above discussion, we have assumed that the underlying data subspace V is known a priori, or we can calculate $P_{V^{\perp}}$ directly. However, in most cases, the only information we have is a set of resolved state variables \mathbf{u}_i s. Then, we can use standard dimension reduction methods such as principal component analysis [19] to obtain a subspace V, which can be thought of as an approximation of the data subspace. The loss objective (3.8) can thus be calculated.

3.2. Algorithm in the general form. The discussion above applies to linear dynamics where the data also lies in a linear subspace. In this subsection, we generalize it to non-linear cases and state the general form of our algorithm.

Let us return to our original formulation of the task (2.1), where we have a dataset $\{(\mathbf{u}_1, \mathbf{y}_1, t_1), (\mathbf{u}_2, \mathbf{y}_2, t_2), \cdots, (\mathbf{u}_N, \mathbf{y}_N, t_N)\}$. As before, we assume that the resolved variable \mathbf{u} lies on a l-dimensional manifold $\mathcal{M} \subset \mathbb{R}^m$ in the configuration space and the estimator $\phi_{\theta}(\mathbf{u}, t)$ achieves high accuracy along this manifold while it has no guarantee outside the manifold. The key difference between the general and the linear dynamics is that \mathcal{M} may not be linear and we do not have a linear projection onto it.

To resolve this, we leverage an autoencoder to represent the data manifold structure: we learn two neural networks $E:\mathbb{R}^m\to\mathbb{R}^l$ (encoder) and $D:\mathbb{R}^l\to\mathbb{R}^m$ (decoder) to represent the manifold. E,D are simultaneously optimized to minimize the reconstruction error

(3.9)
$$\min_{E,D} \frac{1}{N} \sum_{i=1}^{N} F^{2}(\mathbf{u}_{i}), \quad F(\mathbf{u}_{i}) := \|\mathbf{u}_{i} - D(E(\mathbf{u}_{i}))\|_{2}.$$

Omitting optimization issues, we can assume that after the training, the function F vanishes on M and a greater value of F implies a greater deviation to the manifold. Thus F can be used as an indicator of distribution shift and is used in all the figures in this paper to quantify it.

The nonlinear analog of the regularization term in (3.8) should be the projection to the normal space $N_{\mathbf{u}_i}\mathcal{M}=T_{\mathbf{u}_i}^{\perp}\mathcal{M}$ at \mathbf{u}_i . However, constructing this projection operator would require a highly accurate optimized decoder map [26] so that $dD_{\mathbf{z}_i}(\mathbf{e}_i), i=1,...,l$ forms a basis of the tangent space $T_{\mathbf{u}_i}\mathcal{M}$. Here $dD_{\mathbf{u}_i}$ is the differential of the mapping D at \mathbf{z}_i and $\{\mathbf{e}_i, i=1,...l\}$ is the standard basis of \mathbb{R}^l . To reduce the computational cost, we pick the normal vector $\nabla F(\mathbf{u}_i) \in N_{\mathbf{u}_i}\mathcal{M}$ and use $(\nabla F(\mathbf{u}_i))^T L(\mathbf{u}_i, \phi_{\theta}(\mathbf{u}_i), t_i)$ to measure the deviation of the velocity along this normal direction. The fact that $\nabla F(\mathbf{u}_i)$ belongs to the normal space of \mathcal{M} at \mathbf{u}_i directly follows from the assumption that F vanishes on \mathcal{M} after training. Moreover, we define $F(\mathbf{u}_i) := \|\mathbf{u}_i - D(E(\mathbf{u}_i))\|_2$ instead of $\|\mathbf{u}_i - D(E(\mathbf{u}_i))\|_2^2$ since the former has an O(1) gradient even near \mathcal{M} while the latter's gradient is of order o(1) near \mathcal{M} which may cause the regularization to be ineffective. The overall regularized loss function of our algorithm in general cases reads (3.10)

$$\min_{\theta} l(\theta) := \min_{\phi_{\theta}} \frac{1}{N} \sum_{i=1}^{N} \left(\|\mathbf{y}_{i} - \phi_{\theta}(\mathbf{u}_{i})\|_{2}^{2} + \lambda \left((\nabla F(\mathbf{u}_{i}))^{T} L(\mathbf{u}_{i}, \phi_{\theta}(\mathbf{u}_{i}), t_{i}) \right)^{2} \right).$$

In the second term, D, E are optimized in advance and frozen during the training of ϕ_{θ} . Since the loss function is regularized by a term that approximately measures the deviation of the velocity vector $L(\mathbf{u}_i, \phi_{\theta}(\mathbf{u}_i), t_i)$ from the tangent space of the data manifold, we name our algorithm "MLHS with tangent-space regularized estimator". The overall algorithm is summarized in subsection 3.2.

There is a subtle difference in our algorithm between linear and nonlinear problems. While in linear case we can directly construct the projection operators onto the orthogonal complement of the linear manifold denoted by $P_{V^{\perp}}$, in nonlinear case each function $F(\mathbf{u})$ only contributes one vector normal to \mathcal{M} . A technique to obtain more normal vectors in the nonlinear case is to have several F_i composed by different autoencoders trained with different architectures or initializations. In this case, the regularization term will have the form

$$(3.11) \quad \lambda \left\| (\nabla \mathbf{F}(\mathbf{u}_i))^T L(\mathbf{u}_i, \phi_{\theta}(\mathbf{u}_i), t_i) \right\|_2^2 = \lambda \sum_{j=1}^K \left((\nabla F_j(\mathbf{u}_i))^T L(\mathbf{u}_i, \phi_{\theta}(\mathbf{u}_i), t_i) \right)^2.$$

Here K is number of normal directions chosen to be penalized with a maximum value $K_{\text{max}} = m - l$. Notice that a greater K also implies a greater computational and memory cost. Throughout our experiment, we will only use one autoencoder to construct the regularization term as this already provides a significant improvement in the simulation accuracy.

Algorithm 3.1 MLHS with tangent-space regularized estimator

input $\{(\mathbf{u}_1, \mathbf{y}_1, t_1), \cdots, (\mathbf{u}_N, \mathbf{y}_N, t_N)\}$, resolved model, penalty strength λ .

- 1: Learn a parameterized model which encodes the structure of training data, i.e. $F_{\eta}(\mathbf{u}) \geq 0, F_{\eta}(\mathbf{u}_k) = 0.$
- 2: Freeze the parameters of this learned model.
- 3: Introduce another surrogate model $\phi_{\theta}(\mathbf{u})$.
- 4: **for** $k = 1, 2, \dots, N$ **do**
- 5: Predict the control variable $\hat{\mathbf{y}}_k = \phi_{\theta}(\mathbf{u}_k)$.
- 6: Calculate the state variable after one-step iteration, i.e. $\hat{\mathbf{u}}_{k+1} = \mathbf{u}_k + \Delta t L(\mathbf{u}_k, \hat{\mathbf{y}}_k, t_k)$.
- 7: Form the loss $l(\theta) = \mathbb{E}\left[\|\mathbf{y}_k \widehat{\mathbf{y}}_k\|_2^2 + \lambda \left((\nabla F(\mathbf{u}_k))^T L(\mathbf{u}_k, \widehat{\mathbf{y}}_k, t_k) \right)^2 \right].$
- 8: Backpropogate to update θ .
- 9: end for

output tangent-space regularized estimator: ϕ_{θ} .

Compared to the literature on distributionally robust optimization (DRO) [44] and numerical analysis of dynamical systems [56, 55], our work takes advantages from both. First, the tangent-space regularized estimator belongs to the family of DRO in the sense that it minimizes the data-driven module of the unresolved part over some perturbations of the data distribution. However, unlike the original DRO which considers all possible perturbations of the data distribution in its neighborhood under some metric, e.g. Wasserstein metric [4], our regularization focus on those perturbations caused by the resolved components of the dynamics. These facilitate us to take advantage of the partial knowledge of the dynamics. As a result, the regularizer we proposed is more problem-specific. Moreover, from the perspective of DRO, our method takes into consideration the behavior of estimator under certain perturbation normal to the data manifold, which is much more tractable than guarding against arbitrary perturbations in distribution space. In section 4, we will implement other benchmarks with general regularizations and compare with our algorithm to illustrate the benefits of combining resolved model information into regularization.

Furthermore, we can understand our method through the lens of the stability analysis of numerical methods for differential equations. The classical result that the least squares estimator converges to the ground truth in the limit of large datasets can be understood as a consistency statement. Here, we show that this is insufficient, and to ensure convergence of the simulated trajectories one needs to also promote stability, and the regularizer proposed by us serves precisely this role. This regularization approach should be contrasted with recent works [62, 6, 29, 16] on learning dynamical models from data which builds stability by specifying the model architecture.

3.3. Interpretation and analysis of the algorithm. Let us now quantify in the linear case, the gains of our algorithm over the ordinary least squares estimator. We first calculate the exact formula for two estimators. Due to the low-rank structure, the OLS algorithm allows infinitely many solutions. Throughout this section, we

make the common choice of the minimum 2-norm solution. Let us first recall two important choices considered in this section will be the OLS estimator and tangent-space regularized estimator, i.e.

(3.12)
$$C_{\text{OLS}} := \arg\min_{C} \frac{1}{N} \sum_{i=1}^{N} \|\mathbf{y}_{i} - C\mathbf{u}_{i}\|_{2}^{2},$$

$$C_{\text{TR}} := \arg\min_{C} \frac{1}{N} \sum_{i=1}^{N} \left(\|\mathbf{y}_{i} - C\mathbf{u}_{i}\|_{2}^{2} + \lambda \|\mathbf{P}_{V^{\perp}}(A + BC)\mathbf{u}_{i}\|_{2}^{2} \right).$$

The next proposition provides the explicit formula for them.

PROPOSITION 3.1. Consider the linear dynamics (3.1), the training data of the variable \mathbf{u} is arranged into a data matrix $\mathbf{U} \in \mathbb{R}^{m \times N}$. Moreover, we assume the column space of \mathbf{U} is contained in a subspace $V \subset \mathbb{R}^m$ with associated projection operator P_V . Then, the OLS estimator and tangent-space regularized estimator for the unresolved component $Y = C^*\mathbf{U} + \epsilon$ have the following form:

(3.13)
$$\widehat{C}_{\text{OLS}} = C^* \, \mathbf{P}_V + \epsilon \mathbf{U}^{\dagger},$$

$$\widehat{C}_{\text{TR}} = (\mathbf{I} + \lambda B^T \, \mathbf{P}_{V^{\perp}} \, B)^{-1} (C^* \, \mathbf{P}_V + \epsilon \mathbf{U}^{\dagger} - \lambda B^T \, \mathbf{P}_{V^{\perp}} \, A P_V).$$

Specifically, in the noiseless scenarios, \widehat{C}_{OLS} recovers C^* on the subspace V but vanishes on its orthogonal complement. To interpret our estimator, let us consider a simpler case with $B = \mathbf{I}, A = \mathbf{0}$. This corresponds to the dynamic $\partial_t \mathbf{u} = C^* \mathbf{u}$, and the regularized estimator is given by

$$\widehat{C}_{\mathrm{TR}} = (\mathbf{I} + \lambda \, \mathbf{P}_{V^{\perp}})^{-1} (C^* \, \mathbf{P}_V + \epsilon \mathbf{U}^{\dagger}) = (\mathbf{I} + \lambda \, \mathbf{P}_{V^{\perp}})^{-1} \widehat{C}_{\mathrm{OLS}}.$$

Therefore, our estimator performs a weighted least squares regression which penalizes the direction perpendicular to the data subspace V, controlled by λ . As the error along this normal direction is the main cause of the distribution shift, it is sensible to reduce it more than the error along the tangent direction, which causes deviations inside the manifold. This shows that the tangent-space regularized estimator does mitigate distribution shift.

Proof of Proposition 3.1. We solve the linear regression problem of the unresolved component analytically. Recall that the solution for the $\min_C \|Y - CU\|_F^2$ is given by $\widehat{C} = YU^\dagger$ where U^\dagger is the pseudo-inverse of the matrix U. Consequently, assume Y is noiseless, i.e. $Y = C^*U$, we have $\widehat{C} = C^*UU^\dagger$. Let us assume the number of data samples is greater than the dimension of the state, i.e. $U \in \mathbb{R}^{n \times N}, n < N$. Then, if U is full rank, i.e. rank U = n, the product UU^\dagger is exactly the identity matrix and \widehat{C} thereby recovers the C^* exactly. However, in our setting, the data is supported on a low dimensional subspace and the data matrix is rank-deficient. Therefore, $UU^\dagger = P_V$, where V is the column space of the data matrix U and also the support set of it. We have $\widehat{C} = C^*P_V$ in this case. Similarly, in the noisy case $Y = C^*U + \epsilon$, we have

$$\widehat{C}_{\rm OLS} = C^* \, \mathbf{P}_V + \epsilon U^{\dagger}.$$

This is the OLS estimator of the unresolved component.

Next, we calculate the formula for tangent-space regularized estimator. The loss function can be reduced to

$$||Y - C\mathbf{U}||_{\mathrm{F}}^{2} + \lambda ||\mathbf{P}_{V^{\perp}}(A + BC)\mathbf{U}||_{\mathrm{F}}^{2}$$

$$(3.16) = \operatorname{Tr}[(Y - C\mathbf{U})^{T}(Y - C\mathbf{U})] + \lambda \operatorname{Tr}[(\mathbf{P}_{V^{\perp}}(A + BC)\mathbf{U})^{T}(\mathbf{P}_{V^{\perp}}(A + BC)\mathbf{U})]$$

$$= \operatorname{Tr}[(Y - C\mathbf{U})^{T}(Y - C\mathbf{U})] + \lambda \operatorname{Tr}[\mathbf{U}^{T}(A + BC)^{T}\mathbf{P}_{V^{\perp}}(A + BC)\mathbf{U}],$$

where we use the fact $P_{V^{\perp}}^T P_{V^{\perp}} = P_{V^{\perp}}$ since $P_{V^{\perp}}$ is a projection. Consequently, the first-order condition is given by

(3.17)
$$C\mathbf{U}\mathbf{U}^{T} - Y\mathbf{U}^{T} + \lambda B^{T} P_{V^{\perp}}(A + BC)\mathbf{U}\mathbf{U}^{T}) = 0.$$

We finally derive our estimator as

(3.18)
$$\widehat{C}_{TR} = (\mathbf{I} + \lambda B^T \mathbf{P}_{V^{\perp}} B) (Y \mathbf{U}^T - \lambda B^T \mathbf{P}_{V^{\perp}} A \mathbf{U} \mathbf{U}^T) (\mathbf{U} \mathbf{U}^T)^{\dagger}$$
$$= (\mathbf{I} + \lambda B^T \mathbf{P}_{V^{\perp}} B)^{-1} (C^* \mathbf{P}_V + \epsilon U^{\dagger} - \lambda B^T \mathbf{P}_{V^{\perp}} A P_V).$$

Remark 3.2. Unlike classical L^1 or L^2 -regularization, the tangent-space regularization does not have the issue of bias-variance trade-off, as both the least square and the regularization terms admit a common minimizer C^* . This is easily observed by plugging in the ground truth C^* to the formula of the regularizer, giving

(3.19)
$$\|\mathbf{P}_{V^{\perp}}(A + BC^*)\mathbf{u}_i\|_2^2 = 0,$$

since \mathbf{u}_i lies in the invariant subspace V of the generator of the dynamics $A + BC^*$. Therefore, increasing λ will mitigate the effect of distribution shift, while at the same time it does not deteriorate the performance of the least squares problem.

Next, we move on to analyze the accuracy gain of the whole simulation algorithm by proving a bound for the error of the simulation trajectory. Denote the statistical error of tangent-space regularized estimator by

$$(3.20) l_{TR}(\widehat{C}) = \mathbb{E}\left(\left\|(C^* - \widehat{C})\mathbf{u}\right\|_2^2 + \lambda \left\|\mathbf{P}_{V^{\perp}}(A + B\widehat{C})\mathbf{u}\right\|_2^2\right).$$

We define the following function which helps simplify the notation

$$(3.21) Q_m(r,T) = m^2 \int_0^T (2+t^{m-1})e^{rt}dt \le 3m^2(1 \lor T^m)(1 \lor e^{rT}), T > 0,$$

where $a \vee b := \max(a, b)$. In all the discussions that follow, we use $\operatorname{eig}_{\max}(A)$ to denote the greatest real part of the eigenvalues of A, i.e.

(3.22)
$$\operatorname{eig}_{\max}(A) = \max\{\Re(s) : \exists v \neq \mathbf{0}, Av = sv\}.$$

As there are several assumptions for the theorem, we state it here for clarity.

Assumption 3.3. We assume both the OLS estimator and TR estimator \widehat{C}_{OLS} , \widehat{C}_{TR} are optimized to have error bounded by δ so that $l_{\text{OLS}}(\widehat{C}_{\text{OLS}}), l_{TR}(\widehat{C}_{TR}) < \delta$ in (3.3) and (3.20). We assume also that $\left\| \mathbf{P}_{V^{\perp}}(A + B\widehat{C}_{\text{TR}}) \mathbf{P}_{V} \right\|_{2} < \sqrt{\delta/\lambda}$.

Without the second assumption, the error bounds in Theorem 3.4 hold with high probability via the observation

$$(3.23) P_{V^{\perp}}(A + B\widehat{C}_{TR}) P_V \mathbf{u} = P_{V^{\perp}} B(\mathbf{I} + \lambda B^T P_{V^{\perp}} B)^{-1} \epsilon \mathbf{U}^{\dagger},$$

and classical theory of linear regression [19] if the training data has variance $\Sigma \ge c\mathbf{I}, c > 0$. In Assumption 3.3, we include this assumption to simplify the proof.

Moreover, we define several notations to simplify the derivation. Let P_1, P_2, P_3 be matrices which transform $A + B\hat{C}$, $(A + B\hat{C}) P_V$, and $P_{V^{\perp}}(A + B\hat{C})$ into their Jordan normal forms respectively and (3.24)

$$c_1 = \operatorname{cond}(P_1),$$
 $c_2 = \operatorname{cond}(P_2),$ $c_3 = \operatorname{cond}(P_3),$ $e_1 = \operatorname{eig}_{\max}(A + B\widehat{C}),$ $e_2 = \operatorname{eig}_{\max}((A + B\widehat{C}) P_V),$ $e_3 = \operatorname{eig}_{\max}(P_{V^{\perp}}(A + B\widehat{C})),$ where $\operatorname{cond}(P)$ denotes the condition number of matrix P .

Theorem 3.4. Under the same setting as Proposition 3.1 and Assumption 3.3, suppose the true trajectory is simulated from an initial condition $\mathbf{u}(0) \in V$ which follows the same distribution of the training data. Then, the errors of OLS and our algorithm is bounded respectively by

$$(3.25) \qquad \mathbb{E} \|\widehat{\mathbf{u}}_{\text{OLS}}(T) - \mathbf{u}(T)\|_{2} \leq c_{1}\sqrt{\delta} \|B\|_{2} Q_{m}(e_{1}, T),$$

$$\mathbb{E} \|\widehat{\mathbf{u}}_{\text{TR}}(T) - \mathbf{u}(T)\|_{2} \leq c_{2}\sqrt{\delta} \Big(\|B\|_{2} Q_{m}(e_{2}, T) + \frac{9m^{4}c_{3}}{\sqrt{\lambda}} \left(1 + 3m^{2}c_{1}\sqrt{\delta} \|B\|_{2} \right) \|A + B\widehat{C}\|_{2} (1 \vee T^{3m})(1 \vee e^{e_{1}T}) \Big).$$

Generally speaking, the exponential factor e_1, e_2 in Q_m may make both bounds loose, especially for large T. This is inevitable as our bounds deal with worst-case scenarios and exponential growth is common in unstable dynamics. If otherwise the dynamic is stable, Q_m will decay exponentially and the bound becomes more effective.

Comparing the two bounds, the first difference is the exponents appearing in the Q-function, i.e. in OLS it is $e_1 = eig_{max}(A + BC)$ while in our algorithm it is $e_2 = \operatorname{eig}_{\max}((A + B\widehat{C}) P_V)$. This is consistent with our expectation as the datadriven surrogate can only be trusted in the subspace V. Therefore, if the ground truth dynamics is unstable in the orthogonal complement V^{\perp} while stable in V, meaning that $e_1 > 0 > e_2$ the error of OLS will be dominated by the error made in V^{\perp} . For tangent-space regularization, the better exponent e_2 clearly mitigates this. This is also observed quantitatively in Figure 3: comparing the error propagations of the TR with $\lambda = 10^7$ with OLS, the rates are very different at the beginning with TR close to e_2 while OLS close to e_1 . However, we need to be careful with the additional terms appearing in the second bound that may have a big e_1 exponent which may lead to the blow-up of the error. However, it also contains an extra factor $\sqrt{\frac{1}{\lambda}}$ and will be much smaller than the counterpart appearing in OLS bound as long as the penalty λ is large enough. This is justified from Figure 3, where we observe TR trajectories with increasing λ s spend more time with a slower rate e_2 , and then saturate to the e_1 -rate.

Proof of Theorem 3.4. In the proof, we will use $\|\cdot\|$ to denote 2-norm for simplification. We start with the error propagation equation which does not take into consideration the low-dimensional structure in the data and dynamics.

(3.26)
$$\frac{d}{dt}(\widehat{\mathbf{u}} - \mathbf{u}) = (A + B\widehat{C})(\widehat{\mathbf{u}} - \mathbf{u}) + B(\widehat{C} - C^*)\mathbf{u},$$

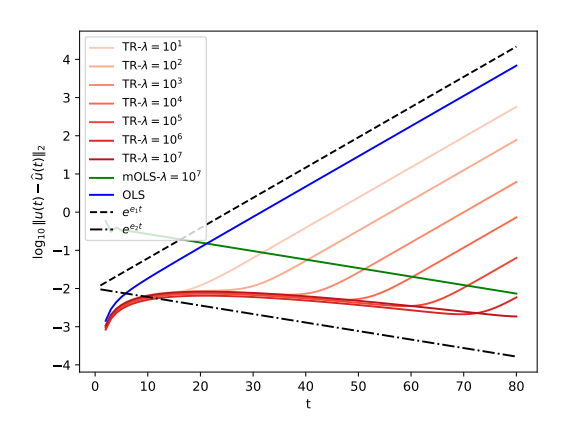


FIG. 3. We compare the simulation error of various estimators in a synthetic linear dynamic where the data subspace $V(V^{\perp})$ is the stable (unstable) manifold. This quantitatively supports our theory from three perspectives: 1). The trajectory error of the OLS simulator coincides with the rate e_1 over the unstable manifold; 2). The trajectory error of our algorithm has two stages, i.e. e_2 -rate at the beginning and e_1 later, which correspond exactly to two parts in (3.25). 3). As $\lambda \to \infty$, the length of the first stage increases, meaning a smaller simulation error.

which can be solved exactly to obtain

(3.27)
$$\widehat{\mathbf{u}}(T) - \mathbf{u}(T) = \int_0^T e^{(A+B\widehat{C})(T-t)} B(\widehat{C} - C^*) \mathbf{u}(t) dt.$$

Therefore, using the bound (proof in supplementary materials) that for $M \in \mathbb{R}^{m \times m}$, $\|e^{Mt}\| \leq \operatorname{cond}(P)m^2(2+t^{m-1})e^{\operatorname{eig}_{\max}(M)t}$, we obtain

(3.28)
$$\mathbb{E} \|\widehat{\mathbf{u}}_{\text{OLS}}(T) - \mathbf{u}(T)\| \leq \int_0^T \left\| e^{(A+B\widehat{C})(T-t)} \right\| \|B\| \mathbb{E} \left\| (\widehat{C} - C^*)\mathbf{u}(t) \right\| dt$$
$$\leq c_1 \sqrt{\delta} \|B\| Q_m(e_1, T) \lesssim \sqrt{\delta} Q_m(e_1, T).$$

Notice that this bound also holds for \mathbf{u}_{TR} as it only requires $\mathbb{E} \| (C_{TR} - C^*) \mathbf{u}(t) \| < \delta$ which is guaranteed by our assumption for l_{TR} . Next, for tangent-space regularization, we need to take into account the existence of the low-dimensional subspace V and the projection operator P_V . Recall the decomposition of the error propagated dynamics

$$(3.29) \quad \frac{d}{dt}(\widehat{\mathbf{u}} - \mathbf{u}) = (A + B\widehat{C}) P_V(\widehat{\mathbf{u}} - \mathbf{u}) + B(\widehat{C} - C^*) \mathbf{u} + (A + B\widehat{C})(\widehat{\mathbf{u}} - P_V \widehat{\mathbf{u}}),$$

and the integration formula for the propagation error (3.6). We need to control the term $P_{V^{\perp}} \hat{\mathbf{u}}(t) = \hat{\mathbf{u}}(t) - P_V \hat{\mathbf{u}}(t)$ originating from the subspace decomposition. (3.30)

$$\frac{d}{dt} \mathbf{P}_{V^{\perp}} \widehat{\mathbf{u}} = \mathbf{P}_{V^{\perp}} (A + B\widehat{C}) \mathbf{P}_{V^{\perp}} \widehat{\mathbf{u}} + \mathbf{P}_{V^{\perp}} (A + B\widehat{C}) \mathbf{P}_{V} (\widehat{\mathbf{u}} - \mathbf{u}) + \mathbf{P}_{V^{\perp}} (A + B\widehat{C}) \mathbf{u},$$

whose solution can be organized as (3.31)

$$\mathbf{P}_{V^{\perp}} \widehat{\mathbf{u}}(T)$$

$$= \ \int_0^T e^{\mathbf{P}_{V^\perp}(A+B\widehat{C})(T-t)} \left(\mathbf{P}_{V^\perp}(A+B\widehat{C}) \, \mathbf{P}_{V} \left(\widehat{\mathbf{u}}(t) - \mathbf{u}(t) \right) + \mathbf{P}_{V^\perp}(A+B\widehat{C}) \mathbf{u}(t) \right) dt.$$

Now, using the Assumption 3.3, one has

$$\mathbb{E} \| \mathbf{P}_{V^{\perp}} \left(\widehat{\mathbf{u}}_{TR}(T) \right) \| \\
\leq c_{3} \sqrt{\frac{\delta}{\lambda}} \left(Q_{m}(e_{3}, T) + m^{2} \int_{0}^{T} e^{(T-t)e_{3}} (2 + (T-t)^{m-1}) \mathbb{E} \| \widehat{\mathbf{u}}_{TR}(t) - \mathbf{u}(t) \| \right) \\
\leq c_{3} \sqrt{\frac{\delta}{\lambda}} \left(3m^{2} (1 \vee T^{m}) (1 \vee e^{e_{3}T}) + 9m^{4} c_{1} \sqrt{\delta} \| B \| (1 \vee T^{2m}) (1 \vee e^{e_{1}T}) \right) \\
\leq 3m^{2} c_{3} \sqrt{\frac{\delta}{\lambda}} \left(1 + 3m^{2} c_{1} \sqrt{\delta} \| B \| \right) (1 \vee T^{2m}) (1 \vee e^{e_{1}T}).$$

In the third line, we use the bound (3.28). Now we plug in the bounds of $P_{V^{\perp}} \hat{\mathbf{u}}_{TR}(T)$ to the error propagation equation and obtain the following bound

(3.33)
$$\mathbb{E} \|\widehat{\mathbf{u}}_{TR}(T) - \mathbf{u}(T)\| \le c_2 \sqrt{\delta} \Big(\|B\| Q_m(e_2, T) + \frac{9m^4c_3}{\sqrt{\lambda}} \Big(1 + 3m^2c_1\sqrt{\delta} \|B\| \Big) \|A + B\widehat{C}\| (1 \vee T^{3m})(1 \vee e^{e_1 T}) \Big).$$

Remark 3.5. Recall our definition of the distribution shift in (2.10). In the proof, assuming $e_1 > 0 > e_2$, we obtain the following estimates of the simulation error of OLS and our algorithm:

(3.34)
$$\mathbb{E} \| \mathbf{P}_{V^{\perp}} \left(\widehat{\mathbf{u}}_{\mathrm{OLS}}(T) \right) \| = O((1 \vee T^{m})(1 \vee e^{e_{1}T})),$$

$$\mathbb{E} \| \mathbf{P}_{V^{\perp}} \left(\widehat{\mathbf{u}}_{\mathrm{TR}}(T) \right) \| = O(\frac{(1 \vee T^{3m})(1 \vee e^{e_{1}T})}{\sqrt{\lambda}}).$$

Therefore, if we define

$$(3.35) d(\rho, \widehat{\rho}) = \left| \mathbb{E} \left\| \mathbf{P}_{V^{\perp}} \mathbf{u} \right\| - \mathbb{E} \left\| \mathbf{P}_{V^{\perp}} \widehat{\mathbf{u}} \right\| \right|, \quad \mathbf{u} \sim \rho, \widehat{\mathbf{u}} \sim \widehat{\rho},$$

we conclude that the OLS algorithm suffers from distribution shift as $P_{V^{\perp}}\mathbf{u} = \mathbf{0}$ while our algorithm can mitigate this issue by choosing a large penalty λ , which is also observed quantitatively in Figure 3. Although this constant may be exponentially large over T in unstable linear dynamics, our numerical experiments in the next section imply that λ needs not to be very large practically.

4. Numerical experiments. In this section, we present numerical experiments which illustrate the effect of the tangent-space regularized algorithm presented in subsection 3.2. We use the experiments to illustrate two phenomena. The first demonstrates the effectiveness of our algorithm, which we test over reaction-diffusion equations and the incompressible Navier-Stokes equation, and compare with benchmark algorithms using the least squares, as well as simple regularizations that do not account for the structure of the resolved dynamics or the data manifold. For the second goal, we show that our method brings more significant improvements in problems with severe distribution shifts. This is demonstrated on the same family of PDEs, i.e. reaction-diffusion equations with varying diffusion coefficients and the Navier-Stokes equation with different Reynolds numbers. These varying parameters can be understood - as we show numerically - as quantitative indicators of the severity of distribution shift. The implementation of our method and experiment reproduction is found in the repository [65].

4.1. Tangent-space regularized algorithm improves simulation accuracy. We first show that the proposed algorithm can be advantageous in several prototypical machine-learning augmented scientific computing applications.

In the first experiment, we use the FitzHugh-Nagumo reaction-diffusion equation (2.11) as the test case of our algorithm. The resolved-unresolved structure is the coarse-fine grid correction structure discussed in subsection 2.2. This helps us obtain high-fidelity simulation results by combining a low-fidelity numerical solver with a fast neural network surrogate model for correction. Here we choose $\alpha = 0.01$, $\beta = 1.0$, $D = \begin{pmatrix} \gamma & 0 \\ 0 & 2\gamma \end{pmatrix}$, $\gamma \in \{0.05, 0.10, 0.15, 0.20, 0.25\}$ in the simulation which guarantees the existence of Turing patterns. The initial condition \mathbf{u}_0 is generated by i.i.d. sampling from a normal distribution $u(x,y,0), v(x,y,0) \sim \mathcal{N}(0,1)$. This system is known to have dynamic spatial patterns where initial smaller clusters gradually transform and merge to form bigger clusters according to the balance between diffusion and reaction effects [36]. In literature, the importance of the sampling procedure is also emphasized, and various adaptive sampling methods based on error and particle methods are studied in [12, 60, 66].

Now, we explain how the training data is prepared. Recall that in (2.6) we discussed the hybrid simulation structure for a correction procedure under a pair of coarse and fine mesh:

(4.1)
$$\begin{cases} \mathbf{u}_{k+1}^{2n} = L(\mathbf{u}_k^{2n}, \mathbf{y}_k^{2n}) = I_n^{2n} \circ f_n(R_{2n}^n(\mathbf{u}_k^{2n})) + \mathbf{y}_k^{2n}, \\ \mathbf{y}_k^{2n} = \phi(\mathbf{u}_k^{2n}). \end{cases}$$

The mapping ϕ between the fine grid state \mathbf{u}_k^{2n} to the correction term \mathbf{y}_k^{2n} is the unresolved model we desire to learn. Here I_n^{2n}, R_{2n}^n are fixed restriction and interpolation operators between two meshes, i.e.

$$(4.2) R_{2n}^n : \mathbb{R}^{2n \times 2n} \to \mathbb{R}^{n \times n}, \mathbf{u}_{ij}^n = \frac{\mathbf{u}_{2i,2j}^{2n} + \mathbf{u}_{2i,2j+1}^{2n} + \mathbf{u}_{2i+1,2j}^{2n} + \mathbf{u}_{2i+1,2j+1}^{2n}}{4},$$

$$I_{2n}^n : \mathbb{R}^{n \times n} \to \mathbb{R}^{2n \times 2n}, \mathbf{u}_{2i,2j}^{2n} = \mathbf{u}_{2i,2j+1}^{2n} = \mathbf{u}_{2i+1,2j}^{2n} = \mathbf{u}_{2i+1,2j+1}^{2n} = \mathbf{u}_{ij}^{n}.$$

To obtain training data for $\mathbf{u}_n^t, \mathbf{u}_{2n}^t$, we simulate (2.11) (with the same initial condition) on two meshes of sizes 64×64 and 128×128 respectively, with time step $\Delta t = 0.01, N_{\text{step}} = T/\Delta t = 100$, using a second-order Crank-Nicolson scheme. It remains to calculate the labels for the training data, i.e. $\mathbf{y}_k^{2n} = \phi(\mathbf{u}_k^{2n})$. These are obtained by using the first half of the (4.2). Finally, we pair them together to form the training data $\{(\mathbf{u}_n^1, \mathbf{y}_n^1), \cdots, (\mathbf{u}_n^N, \mathbf{y}_n^N)\}$. The data here is different from the one introduced in subsection 2.3 since the system is autonomous, so we do not include time indices. To summarize, the training data contains two patches of field component patterns of size $100 \times 128 \times 128$ corresponding to \mathbf{u}, \mathbf{v} respectively and two patches $\mathbf{y}_u, \mathbf{y}_v$ of the same shape and generated according to (4.2).

The baseline algorithms we implemented to compare with ours is ϕ_{OLS} , which minimizes the mean-squared error on the training data, i.e.

(4.3)
$$\phi_{\text{OLS}} = \arg\min \mathbb{E}_{\mathbf{u} \sim \rho_0} \|\phi_{\theta}(\mathbf{u}) - \phi(\mathbf{u})\|_2^2,$$

where we use ρ_0 to denote the distribution of the field variable. The corresponding numerical results are labeled by "OLS".

We summarize the comparison results in Figure 4. Here, solid lines represent the errors along the trajectories and dashed lines represent the distribution shift. The

20 Zhao and li

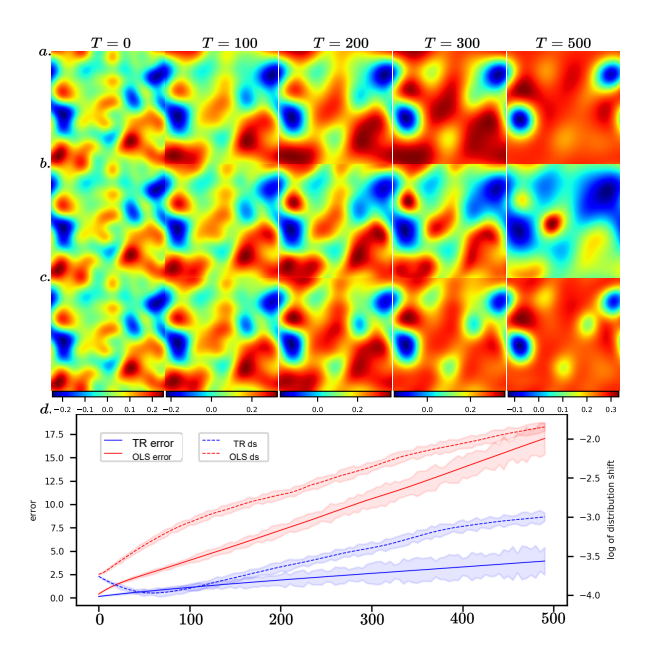


FIG. 4. Simulation of reaction-diffusion equations and configurations at time step: 0, 100, 200, 300, 500, (a) ground truth; (b) simulated fluid field using OLS estimator; (c) simulated fluid field using TR estimator. (d) is the comparison of the ordinary least squares and regularized one on reaction-diffusion equations: the solid line represents the averaged error along the trajectory and the dashed line represents the averaged distribution shift calculated using function F defined in (3.9). The shadow part is the standard deviation in ten random experiments with different training and testing data. Both the error and the distribution shift increase at a lower speed in TR simulation than in OLS simulations. This suggests that the better performance of TR algorithm in reaction-diffusion equations is partially caused by improving the distribution shift issue.

shaded part is the standard deviation over ten random experiments with different splits of the training and testing data. As can be observed, compared to our method the OLS baseline incurs greater errors and distribution shifts. Moreover, this difference increases with time. In contrast, consistent with our analysis in the simplified setting, our algorithm mitigates both the distribution shift and the trajectory error.

Next, we consider the Navier-Stokes equation (2.3) as the test case of our algorithm subsection 3.2. In this case, the resolved model is an explicit scheme to evolve the velocity field while unresolved model is calculated via a fast CNN surrogate, which can accelerate the simulation for large grid systems. The simulation domain is rectangular with an aspect ratio 1/4. On the upper and lower boundary we impose the no-slip boundary condition on the velocity and on the inlet, i.e. x = 0 we specify the velocity field \mathbf{u} . Moreover, at the outlet, i.e. x = n we pose zero-gradient conditions on both the horizontal velocity and pressure, i.e. $\frac{\partial p}{\partial n} = \frac{\partial u}{\partial n} = 0$. The inflow boundary is defined according to following functional forms:

(4.4)
$$\mathbf{u}(0,y,t) = \begin{pmatrix} u(0,y,t) \\ v(0,y,y) \end{pmatrix} = \begin{pmatrix} \exp\{-50(y-y_0)^2\} \\ \sin t \cdot \exp\{-50(y-y_0)^2\} \end{pmatrix}$$

The training configuration is calculated using the projection method [8] with a staggered grid, i.e. the pressure is placed at the center of each cell and horizontal (vertical) velocity is placed at vertical (horizontal) edge of each cell. The jet location y_0 is selected from 0.3 to 0.7 uniformly. Again, we compare the performance of our algorithm and the OLS method. As illustrated in Figure 5, naively using OLS to estimate the unresolved models will generally lead to an error blow-up, whereas using our regularized estimator we can obtain a reasonable simulation along the whole time horizon. Moreover, the trend of the trajectory error fits that of the distribution shift. In particular, the error and distribution shift blow-ups occur simultaneously. Our algorithm again decreases the trajectory error by mitigating the distribution shift problem. Moreover, the blow-up of the error in the simulated dynamics is not explained in Theorem 3.4 as the theory is established for linear dynamics while finite-time blow-up is known to be a special feature of nonlinear dynamics.

We also notice the unphysical noise appearing in the numerical experiments of the Navier-Stokes equation, i.e. Figure 5 b. which is also observed in [31, 32, 61, 43] when performing data-driven RANS modeling. While this is not the main focus of this paper which deals with the distribution shift issue, we observe that such noise mainly occurs in the simulation of the NS equation instead of reaction-diffusion equations. Therefore, one possible explanation is that this noise is caused by transport-dominated equations and diffusion can reduce this noise in diffusion-dominated equations.

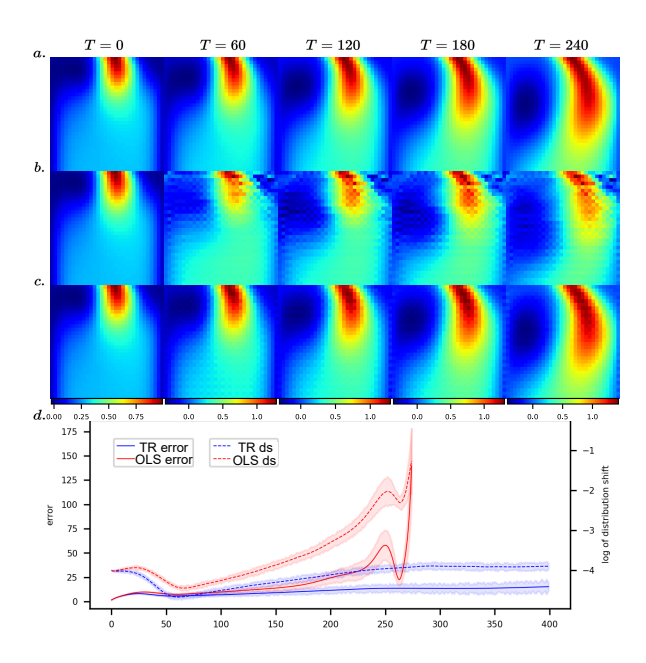


FIG. 5. Simulation of the Navier-Stokes equation and configurations at time step: 0, 60, 120, 180, 240, (a) ground truth; (b) simulated fluid velocity field using OLS estimator; (c) simulated fluid velocity field using TR estimator; (d) the comparison of the OLS estimator and the regularized one. The solid lines represent the trajectory error and the dashed lines represent the distribution shift calculated usingusing function F defined in (3.9). We observe that the OLS estimator leads to error (and DS) blow-up at around 270 steps, while our method remains stable. Again, the trends of error and distribution shift are highly correlated, and our method that controls distribution shift leads to error control, consistent with our analyses.

The machine-learning augmented NS simulations appear to have a greater degree of distribution shift, and our method has a relatively stronger benefit in this case. This suggests that our method is most beneficial in problems where the intrinsic distribution shift is severe. In the next subsection, we will study this more systematically by testing our method on the reaction-diffusion equations with varying

22 Zhao and li

diffusion coefficient γ and Navier-Stokes equations with varying Reynolds numbers.

4.2. Performance under distribution shift of different magnitudes. We now demonstrate concretely that our method brings more significant improvements when the intrinsic distribution shift is more severe. Intuitively speaking, since our algorithm penalizes the deviation of the simulated trajectories to the data manifold while OLS ignores this, it would be reasonable to expect that our algorithm will outperform OLS more in problems where such deviations are large. A sanity check showing different distribution shift extents under different parameters is provided in Figure 3 of supplementary materials.

Here, we introduce two more baselines for ablation studies. Compared with the OLS algorithm, these algorithms both add some regularization to the loss function while their regularizations are general and not dynamics-specific compared to our regularization. Consequently, any improved performance in our algorithm over these regularized algorithms suggest that targeted regularization, which takes into account the structure of the resolved part, effectively balances accuracy and stability.

The first baseline regularizes the original least squares objective by a term that quantifies some complexity of the network model, e.g.

(4.5)
$$\phi_{\text{mOLS}} = \arg\min \mathbb{E}_{\mathbf{u} \sim \rho_0} \|\phi_{\theta}(\mathbf{u}) - \phi(\mathbf{u})\|_2^2 + \lambda \|\theta\|_2^2.$$

Here the naive L^2 regularized algorithm is implemented by adjusting the weight decay [34] parameter of the Adam solver during the training process. The corresponding numerical results are labeled by "mOLS" ("m" for modified).

The second baseline adds noise to the training data during training, which can be formulated as

(4.6)
$$\phi_{\text{aOLS}} = \arg\min \mathbb{E}_{\mathbf{u} \sim \rho_{\xi}} \|\phi_{\theta}(\mathbf{u}) - \phi(\mathbf{u})\|_{2}^{2}.$$

Notice that the training data follows the distribution $\rho_{\epsilon} = \rho_0 * \xi$ where * denotes the convolution operator and ξ is some random noise which we take to be Gaussian random variables with an adjustable variance. In our implementation, we generate the noise and add it to the input during each epoch, so the inputs are not the same across epochs. Moreover, this noise ξ should be distinguished from the observational noise ϵ we introduced in section 3. This method has been used in several previous works [54, 40] to improve stability and prevent the error from accumulating too fast. As this technique is similar to adversarial attack and data augmentation [52, 14, 13], we name this estimator and algorithm as "aOLS" ("a" stands for adversarial). We slightly abuse the terminology here by naming this random perturbation as some kind of adversarial attack.

In Table 1, we test the algorithms under different diffusion coefficient $\gamma=0.05$, 0.10, 0.15, 0.20, 0.25. We calculate the relative trajectory error at time T=1000, i.e. $\frac{\|\mathbf{u}_k-\widehat{\mathbf{u}}_k\|_2}{\|\mathbf{u}_k\|_2}$ over ten random splits of the training and test data. The last row calculates the performance difference between our method and the OLS baseline. We observe that under almost all the settings our method out-performs OLS, mOLS, aOLS baselines, and comparing horizontally, we see that the relative improvement decreases with γ , as the diffusion term mitigates the distribution shift.

We now consider the Navier-Stokes equation. Since the baseline method quickly leads to error blow-up, we use another comparison criterion. We define a stopping time $t_K = \arg\max_t \frac{\|\mathbf{u}_t - \hat{\mathbf{u}}_t\|_2}{\|\mathbf{u}_t\|_2} \leq K$ where K is an error threshold to be determined during the experiments. We calculate the first time the trajectory error reaches a

 ${\it TABLE~1} \\ Performance~on~reaction-diffusion~equations~over~10~experiments.$

	$\gamma = 0.05$	$\gamma = 0.10$	$\gamma = 0.15$	$\gamma = 0.20$	$\gamma = 0.25$
		grid size:	64×64		
OLS	8.40E + 1	1.04E + 1	8.99E+0	2.22E+0	6.78E-1
mOLS	8.90E+0	9.22E+0	1.41E+0	2.26E+0	9.98E-1
aOLS	3.57E + 1	4.00E+1	2.40E+0	1.79E+0	1.06E+0
TR	1.23E-1	1.06E-1	1.38E-1	1.85E-1	2.15E-1
Diff	99.9%	99.0%	98.5%	91.7%	68.3%
		grid size:	128×128		
OLS	4.10E+2	8.18E+1	5.11E+1	4.88E+0	2.25E+0
mOLS	2.40E+1	3.20E+1	2.20E+0	1.07E+1	1.25E+0
aOLS	1.46E+2	2.58E+2	8.69E+0	3.30E+0	1.79E+0
TR	2.79E-1	1.66E-1	2.42E-1	1.81E-1	1.91E-1
Diff	99.9%	99.8%	99.5%	96.3%	91.5%

	Re = 100	Re = 200	Re = 300	Re = 400	Re = 500
		grid size:	128×32		_
OLS	435 ± 15	301 ± 20	240 ± 12	177 ± 17	120 ± 7
mOLS	420 ± 12	333 ± 14	254 ± 12	204 ± 9	210 ± 7
aOLS	477 ± 25	392 ± 31	450 ± 23	239 ± 25	321 ± 20
TR	506 ± 18	497 ± 28	482 ± 29	442 ± 21	452 ± 13
		grid size:	256×64		
OLS	602 ± 38	571 ± 35	355 ± 25	301 ± 11	148 ± 22
mOLS	623 ± 18	531 ± 26	489 ± 20	417 ± 10	298 ± 9
aOLS	651 ± 48	601 ± 42	595 ± 39	378 ± 31	398 ± 32
TR	636 ± 35	602 ± 28	585 ± 23	422 ± 35	402 ± 28

threshold under different Reynolds numbers and different mesh sizes. The results are shown in Table 2. Under almost all the scenarios, our method outperforms all the baseline algorithms by a larger t_K . This validates the effectiveness of our algorithm. Comparing Table 2 horizontally, one finds that the improvement of our method is also increasing concerning the Reynolds number. As the flow field generally becomes more complex (and sensitive) with increasing Reynolds number, our method is expected to bring bigger improvements. This is consistent with our experiments.

5. Conclusion. In this paper, we establish a theoretical framework for machine-learning augmented hybrid simulation problems, where a data-driven surrogate is used to accelerate traditional simulation methods. We identify the cause and effect of distribution shift, i.e. the empirically observed phenomenon that the simulated dynamics may be driven away from the support of the training data due to systematic errors introduced by the data-driven surrogate and magnified by the resolved components of the dynamics. Based on this, we propose a tangent-space regularized algorithm

for training the surrogate for the unresolved part, which incorporates the resolved model information to control deviations from the true data manifold. In the case of linear dynamics, we show our algorithm is provably better than the traditional training method based on ordinary least squares. Then, we validate our algorithm in numerical experiments, including Turing instabilities in reaction-diffusion equations and fluid flow. In both cases, our method outperforms baselines by better mitigating distribution shift, thus reducing trajectory error. Important problems such as different discretizations for training and simulating, and applications to turbulent flow simulations are beyond the scope of this paper and left for future study.

Acknowledgements. The research work presented is supported by the National Research Foundation, Singapore, under the NRF fellowship (project No. NRF-NRFF13-2021-0005). We thank Zhixuan Li, Sohei Arisaka, Jiequn Han for valuable discussions.

REFERENCES

- G. Alfonsi, Reynolds-averaged navier-stokes equations for turbulence modeling, Applied Mechanics Reviews, 62 (2009).
- [2] S. Arisaka and Q. Li, Principled acceleration of iterative numerical methods using machine learning, in Proceedings of the 40th International Conference on Machine Learning, ICML'23, JMLR.org, 2023.
- [3] M. BACHMAYR AND A. COHEN, Kolmogorov widths and low-rank approximations of parametric elliptic pdes, Mathematics of Computation, 86 (2017), pp. 701–724.
- [4] J. Blanchet, K. Murthy, and N. Si, Confidence regions in wasserstein distributionally robust estimation, Biometrika, 109 (2022), pp. 295–315.
- [5] W. L. Briggs, V. E. Henson, and S. F. McCormick, A multigrid tutorial, SIAM, 2000.
- [6] M. CRANMER, S. GREYDANUS, S. HOYER, P. BATTAGLIA, D. SPERGEL, AND S. HO, Lagrangian neural networks, arXiv preprint arXiv:2003.04630, (2020).
- [7] X. Dong, Z. Yu, W. Cao, Y. Shi, and Q. Ma, A survey on ensemble learning, Frontiers of Computer Science, 14 (2020), pp. 241–258.
- [8] W. E AND J.-G. Liu, Projection method i: convergence and numerical boundary layers, SIAM journal on numerical analysis, (1995), pp. 1017–1057.
- [9] H. EIVAZI, H. VEISI, M. H. NADERI, AND V. ESFAHANIAN, Deep neural networks for nonlinear model order reduction of unsteady flows, Physics of Fluids, 32 (2020).
- [10] A. FARAHANI, S. VOGHOEI, K. RASHEED, AND H. R. ARABNIA, A brief review of domain adaptation, Advances in Data Science and Information Engineering: Proceedings from ICDATA 2020 and IKE 2020, (2021), pp. 877–894.
- [11] C. Fefferman, S. Mitter, and H. Narayanan, *Testing the manifold hypothesis*, Journal of the American Mathematical Society, 29 (2016), pp. 983–1049.
- [12] Z. GAO, L. YAN, AND T. ZHOU, Failure-informed adaptive sampling for pinns, SIAM Journal on Scientific Computing, 45 (2023), pp. A1971–A1994, https://doi.org/10.1137/22M1527763, https://doi.org/10.1137/22M1527763, https://doi.org/10.1137/22M1527763.
- [13] I. GOODFELLOW, Y. BENGIO, AND A. COURVILLE, *Deep Learning*, MIT Press, 2016. http://www.deeplearningbook.org.
- [14] I. GOODFELLOW, J. POUGET-ABADIE, M. MIRZA, B. XU, D. WARDE-FARLEY, S. OZAIR, A. COURVILLE, AND Y. BENGIO, Generative adversarial nets, in Advances in Neural Information Processing Systems, Z. Ghahramani, M. Welling, C. Cortes, N. Lawrence, and K. Weinberger, eds., vol. 27, Curran Associates, Inc., 2014, https://proceedings.neurips.cc/paper_files/paper/2014/file/5ca3e9b122f61f8f06494c97b1afccf3-Paper.pdf.
- [15] I. GOODFELLOW, J. POUGET-ABADIE, M. MIRZA, B. XU, D. WARDE-FARLEY, S. OZAIR, A. COURVILLE, AND Y. BENGIO, Generative adversarial networks, Communications of the ACM, 63 (2020), pp. 139–144.
- [16] S. Greydanus, M. Dzamba, and J. Yosinski, Hamiltonian neural networks, Advances in neural information processing systems, 32 (2019).
- [17] J.-L. GUERMOND, P. MINEV, AND J. SHEN, An overview of projection methods for incompressible flows, Computer methods in applied mechanics and engineering, 195 (2006), pp. 6011– 6045.

- [18] T. HASTIE, R. TIBSHIRANI, J. FRIEDMAN, T. HASTIE, R. TIBSHIRANI, AND J. FRIEDMAN, Overview of supervised learning, The elements of statistical learning: Data mining, inference, and prediction, (2009), pp. 9–41.
- [19] T. HASTIE, R. TIBSHIRANI, J. H. FRIEDMAN, AND J. H. FRIEDMAN, The elements of statistical learning: data mining, inference, and prediction, vol. 2, Springer, 2009.
- [20] P. Holmes, J. L. Lumley, G. Berkooz, and C. W. Rowley, Turbulence, Coherent Structures, Dynamical Systems and Symmetry, Cambridge Monographs on Mechanics, Cambridge University Press, 2 ed., 2012.
- [21] P. J. Holmes, J. L. Lumley, G. Berkooz, J. C. Mattingly, and R. W. Wittenberg, Low-dimensional models of coherent structures in turbulence, Physics Reports, 287 (1997), pp. 337–384.
- [22] R. HUANG, R. LI, AND Y. XI, Learning optimal multigrid smoothers via neural networks, SIAM Journal on Scientific Computing, (2022), pp. S199–S225.
- [23] A. HUSSEIN, M. M. GABER, E. ELYAN, AND C. JAYNE, Imitation learning: A survey of learning methods, ACM Comput. Surv., 50 (2017), https://doi.org/10.1145/3054912, https://doi. org/10.1145/3054912.
- [24] D. P. KINGMA AND J. BA, Adam: A method for stochastic optimization, arXiv preprint arXiv:1412.6980, (2014).
- [25] P. W. Koh, S. Sagawa, H. Marklund, S. M. Xie, M. Zhang, A. Balsubramani, W. Hu, M. Yasunaga, R. L. Phillips, I. Gao, et al., Wilds: A benchmark of in-the-wild distribution shifts, in International Conference on Machine Learning, PMLR, 2021, pp. 5637–5664.
- [26] M. KVALHEIM AND E. SONTAG, Why should autoencoders work?, Transactions on Machine Learning Research.
- [27] Y. LECUN, Y. BENGIO, AND G. HINTON, Deep learning, nature, 521 (2015), pp. 436-444.
- [28] K. LEE AND K. T. CARLBERG, Model reduction of dynamical systems on nonlinear manifolds using deep convolutional autoencoders, Journal of Computational Physics, 404 (2020), p. 108973.
- [29] B. Lin, Q. Li, And W. Ren, A data driven method for computing quasipotentials, arXiv preprint arXiv:2012.09111, (2020).
- [30] L. Lin, J. Lu, and L. Ying, Numerical methods for kohn-sham density functional theory, Acta Numerica, 28 (2019), pp. 405–539.
- [31] J. Ling, A. Kurzawski, and J. Templeton, Reynolds averaged turbulence modelling using deep neural networks with embedded invariance, Journal of Fluid Mechanics, 807 (2016), pp. 155–166.
- [32] J. LING AND J. TEMPLETON, Evaluation of machine learning algorithms for prediction of regions of high reynolds averaged navier stokes uncertainty, Physics of Fluids, 27 (2015), p. 085103.
- [33] L. Ljung, System identification, in Signal analysis and prediction, Springer, 1998, pp. 163–173.
- [34] I. LOSHCHILOV AND F. HUTTER, Decoupled weight decay regularization, arXiv preprint arXiv:1711.05101, (2017).
- [35] R. MAULIK, O. SAN, A. RASHEED, AND P. VEDULA, Subgrid modelling for two-dimensional turbulence using neural networks, Journal of Fluid Mechanics, 858 (2019), pp. 122–144.
- [36] J. D. MURRAY AND J. D. MURRAY, Mathematical Biology: II: Spatial Models and Biomedical Applications, vol. 3, Springer, 2003.
- [37] H. NARAYANAN AND S. MITTER, Sample complexity of testing the manifold hypothesis, Advances in neural information processing systems, 23 (2010).
- [38] A. PASZKE, S. GROSS, F. MASSA, A. LERER, J. BRADBURY, G. CHANAN, T. KILLEEN, Z. LIN, N. GIMELSHEIN, L. ANTIGA, ET AL., Pytorch: An imperative style, high-performance deep learning library, Advances in neural information processing systems, 32 (2019).
- [39] C. Pedersen, L. Zanna, J. Bruna, and P. Perezhogin, Reliable coarse-grained turbulent simulations through combined offline learning and neural emulation, 2023, https://arxiv. org/abs/2307.13144.
- [40] T. Pfaff, M. Fortunato, A. Sanchez-Gonzalez, and P. W. Battaglia, Learning mesh-based simulation with graph networks, CoRR, abs/2010.03409 (2020), https://arxiv.org/abs/2010.03409, https://arxiv.org/abs/2010.03409.
- [41] F. Pichi, B. Moya, and J. S. Hesthaven, A graph convolutional autoencoder approach to model order reduction for parametrized pdes, arXiv preprint arXiv:2305.08573, (2023).
- [42] S. B. Pope and S. B. Pope, Turbulent flows, Cambridge university press, 2000.
- [43] S. V. POROSEVA, J. D. COLMENARES F, AND S. M. MURMAN, On the accuracy of rans simulations with dns data, Physics of Fluids, 28 (2016), p. 115102.
- [44] H. RAHIMIAN AND S. MEHROTRA, Distributionally robust optimization: A review, arXiv preprint arXiv:1908.05659, (2019).
- [45] P. REN, C. RAO, Y. LIU, Z. MA, Q. WANG, J.-X. WANG, AND H. SUN, Physics-informed deep

- super-resolution for spatiotemporal data, arXiv preprint arXiv:2208.01462, (2022).
- [46] O. Ronneberger, P. Fischer, and T. Brox, U-net: Convolutional networks for biomedical image segmentation, in International Conference on Medical image computing and computer-assisted intervention, Springer, 2015, pp. 234–241.
- [47] S. Ross, G. Gordon, and D. Bagnell, A reduction of imitation learning and structured prediction to no-regret online learning, in Proceedings of the Fourteenth International Conference on Artificial Intelligence and Statistics, G. Gordon, D. Dunson, and M. Dudík, eds., vol. 15 of Proceedings of Machine Learning Research, Fort Lauderdale, FL, USA, 11–13 Apr 2011, PMLR, pp. 627–635, https://proceedings.mlr.press/v15/ross11a.html.
- [48] B. Sanderse, P. Stinis, R. Maulik, and S. E. Ahmed, Scientific machine learning for closure models in multiscale problems: a review, 2024, https://arxiv.org/abs/2403.02913, https://arxiv.org/abs/2403.02913.
- [49] V. SHANKAR, R. MAULIK, AND V. VISWANATHAN, Differentiable turbulence, 2023, https://arxiv.org/abs/2307.03683.
- [50] V. SHANKAR, R. MAULIK, AND V. VISWANATHAN, Differentiable turbulence ii, arXiv preprint arXiv:2307.13533, (2023).
- [51] J. R. Shewchuk, An introduction to the conjugate gradient method without the agonizing pain, 1994.
- [52] C. SHORTEN AND T. M. KHOSHGOFTAAR, A survey on image data augmentation for deep learning, Journal of Big Data, 6 (2019), p. 60, https://doi.org/10.1186/s40537-019-0197-0, https://doi.org/10.1186/s40537-019-0197-0.
- [53] J. P. SLOTNICK, A. KHODADOUST, J. ALONSO, D. DARMOFAL, W. GROPP, E. LURIE, AND D. J. MAVRIPLIS, Cfd vision 2030 study: a path to revolutionary computational aerosciences, 2014.
- [54] K. STACHENFELD, D. B. FIELDING, D. KOCHKOV, M. CRANMER, T. PFAFF, J. GODWIN, C. CUI, S. HO, P. BATTAGLIA, AND A. SANCHEZ-GONZALEZ, Learned coarse models for efficient turbulence simulation, 2022, https://arxiv.org/abs/2112.15275.
- [55] A. STUART AND A. R. HUMPHRIES, Dynamical systems and numerical analysis, vol. 2, Cambridge University Press, 1998.
- [56] A. M. STUART, Numerical analysis of dynamical systems, Acta numerica, 3 (1994), pp. 467–572.
- [57] J. TOMPSON, K. SCHLACHTER, P. SPRECHMANN, AND K. PERLIN, Accelerating eulerian fluid simulation with convolutional networks, in International Conference on Machine Learning, PMLR, 2017, pp. 3424–3433.
- [58] J. Vanschoren, Meta-learning: A survey, arXiv preprint arXiv:1810.03548, (2018).
- [59] R. WANG AND R. YU, Physics-guided deep learning for dynamical systems: A survey, arXiv preprint arXiv:2107.01272, (2021).
- [60] Y. Wen, E. Vanden-Eijnden, and B. Peherstorfer, Coupling parameter and particle dynamics for adaptive sampling in neural galerkin schemes, arXiv preprint arXiv:2306.15630, (2023).
- [61] J. Wu, H. Xiao, R. Sun, and Q. Wang, Reynolds-averaged navier-stokes equations with explicit data-driven reynolds stress closure can be ill-conditioned, Journal of Fluid Mechanics, 869 (2019), pp. 553-586.
- [62] H. Yu, X. Tian, W. E, and Q. Li, Onsagernet: Learning stable and interpretable dynamics using a generalized onsager principle, Physical Review Fluids, 6 (2021), p. 114402.
- [63] L. ZHANG, J. HAN, H. WANG, R. CAR, AND E. WEINAN, Deep potential molecular dynamics: a scalable model with the accuracy of quantum mechanics, Physical review letters, 120 (2018), p. 143001.
- [64] L. Zhang, D.-Y. Lin, H. Wang, R. Car, and E. Weinan, Active learning of uniformly accurate interatomic potentials for materials simulation, Physical Review Materials, 3 (2019), p. 023804.
- [65] J. Zhao and Q. Li, Code repository for mitigating distribution shift in machine-learning augmented hybrid simulation, https://github.com/jiaxi98/ml4dynamics.
- [66] Z. Zhao and Q. Li, Adaptive sampling methods for learning dynamical systems, in Mathematical and Scientific Machine Learning, PMLR, 2022, pp. 335–350.
- [67] Y. ZHIYIN, Large-eddy simulation: Past, present and the future, Chinese journal of Aeronautics, 28 (2015), pp. 11–24.

Appendix A. Linear dynamics.

A.1. Auxiliary results. We provide the proof of the following lemma.

LEMMA A.1. Suppose P is a matrix whose similarity transformation transforms M to its Jordan form. The following bound for $M \in \mathbb{R}^{m \times m}$ holds

$$||e^{Mt}||_2 \le \operatorname{cond}(P)m^2(2+t^{m-1})e^{\operatorname{eig}_{\max}(M)t}.$$

Proof. Writing the Jordan decomposition of the matrix M as

$$(A.1) M = PJP^{-1},$$

where J is the Jordan normal form of M with Jordan block J_1, J_2, \dots, J_k . Then, the exponential can be written as

(A.2)
$$e^{Mt} = Pe^{Jt}P^{-1} = P\operatorname{diag}(e^{J_1t}, \dots, e^{J_kt})P^{-1}.$$

We can bound the matrix norm of the LHS by

(A.3)
$$\|e^{Mt}\|_{2} \le \operatorname{cond}(P) \|e^{Jt}\|_{2} \le \operatorname{cond}(P) \max_{i=1,\dots,k} \|e^{J_{i}t}\|_{2}$$
.

It suffices to estimate the norm of the exponential of a Jordan block. Suppose we have the following Jordan block of shape $m_i \times m_i$

(A.4)
$$J_{i} = \begin{pmatrix} \lambda_{i} & 1 & 0 & \cdots & 0 \\ 0 & \lambda_{i} & 1 & \cdots & 0 \\ \vdots & \vdots & \vdots & \ddots & \vdots \\ 0 & 0 & 0 & \cdots & \lambda_{i} \end{pmatrix}, \quad e^{J_{i}t} = e^{\lambda_{i}t} \begin{pmatrix} 1 & t & t^{2} & \cdots & \frac{t^{m_{i}-1}}{(m_{i}-1)!} \\ 0 & 1 & t & \cdots & \frac{t^{m_{i}-2}}{(m_{i}-2)!} \\ \vdots & \vdots & \vdots & \ddots & \vdots \\ 0 & 0 & 0 & \cdots & 1 \end{pmatrix}.$$

Lastly, we can bound the norm of this exponential as

(A.5)
$$||e^{J_i t}||_2 \le e^{\Re(\lambda_i)t} \sum_{i,j=1}^{m_i} (e^{J_i t})_{ij} \le m_i^2 (1 + t^{m_i - 1}) e^{\Re(\lambda_i)t},$$

which concludes our proof.

A.2. Comparison of different methods over linear dynamics. Here, we compare our method with OLS in a toy linear dynamics in Figure 7. As the OLS estimator does not involve any penalty term, we further introduce the modified OLS (mOLS) with the following objective function

(A.6)
$$l_{mOLS}(\widehat{C}) = \mathbb{E}\left(\left\| (C^* - \widehat{C})\mathbf{u} \right\|_2^2 + \lambda \left\| \widehat{C} \right\|_F^2 \right),$$

to quantitatively compare the performance of estimators with different regularizations. We fix the overall dynamics to be

(A.7)
$$\mathbf{u}_{n+1} = (A + BC)\mathbf{u}_n = F\mathbf{u}_n, \quad F = \begin{pmatrix} 0.95 & 0\\ 0 & 1.2 \end{pmatrix}.$$

In each test case, B is set to be the identity matrix and C is randomly generated with each element following i.i.d. uniform distribution over [0,1]. The initial condition is

sampled from $\mathbf{u}_0 \sim (\mathcal{N}(\mathbf{0},1),0)$, i.e. the first coordinate from i.i.d. standard Gaussian and the second coordinates fixed to 0. It is simple to conclude that all the data will concentrate on the stable manifold $\mathbb{R} \times \{0\}$. The observational noise scale is set to 0.001 and the number of time steps to 50. Based on the trajectories simulated from these initial conditions, we calculate the OLS and TR estimators and their corresponding trajectory error.

The performance of the tangent-space regularized algorithm achieves better performance than the OLS algorithm and mOLS. Meanwhile, as we increase the penalty λ , the error curves become closer to the best rate of the error rate inside the stable manifold. More precisely, we draw the error propagation rates in the stable and unstable manifold using two dashed lines. This result quantitatively supports our theory from three perspectives:

- The trajectory error of the OLS simulator coincides with the rate over the unstable manifold, i.e. e_1 and exhibits exponential blow-up. This supports our error bound for \mathbf{u}_{OLS} .
- The trajectory error of the TR simulator has two stages. At the early stage, the error changes with a rate close to the error rate in the stable manifold, i.e. e₂ < 0 < e₁. At the late stage, the error accumulates at a rate similar to the rate in the unstable manifold and OLS error rate. This implies two components in the error bound for the TR algorithm where the first term dominates at the early stage while the other dominates late dynamics. Moreover, as λ → ∞, the length of the first stage increases, meaning a smaller simulation error.
- Lastly, our TR outperforms the OLS algorithm with L^2 -regularization. Although the rates of error accumulation are similar, the initial error of our algorithm is much smaller than that of regularized OLS, as our estimator is unbiased while the mOLS estimator is biased.

Moreover, We elaborate on the relationship between the long time prediction accuracy with λ in Figure 7. The first observation is that both regularized methods outperform the naive OLS method as regularization penalizes the deviation along the unstable direction. Secondly, the error of mOLS and TR both decrease as regularization becomes stronger. However, as λ becomes larger, the improvement of the mOLS algorithm ceases and cannot achieve better performance than 10^{-3} . This is because regularization $\|\widehat{C}\|_F$ does not distinguish the directions lying inside the manifold containing the true trajectories (here the line parallel to (1,0)) and those pointing outward. Large λ guarantees the components along unstable directions are small and also forces the components along directions inside the manifold to be small, which leads to performance deterioration. However, the proposed TR estimator distinguishes between the directions lying inside and pointing outwards of the manifold and selectively penalizes the latter. Therefore, the error made along the unstable direction is eliminated as $\lambda \to \infty$ while at the same time, the prediction along the tangent space is not affected. This guarantees a continuous improvement of the trajectory prediction for the tangent-space regularized algorithm, outperforming the classical norm-based regularization.

Appendix B. Numerical experiments details. In this section, we first describe how to prepare the training data of reaction-diffusion equations and Navier-Stokes equations. Then, we discuss the experimental details of the neural networks and algorithms.

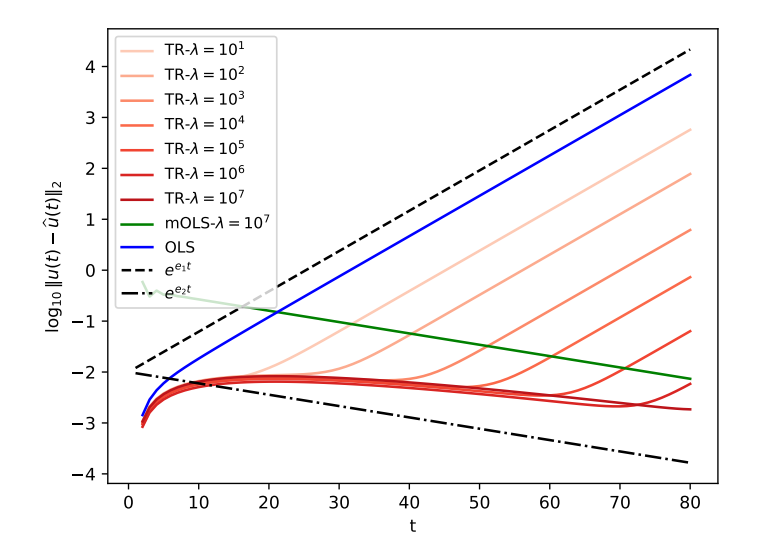


Fig. 6. We compare the simulation error of various estimators in a synthetic linear dynamic where the data subspace $V(V^{\perp})$ is the stable (unstable) manifold. This quantitatively supports our theory from three perspectives: 1). The trajectory error of the OLS simulator coincides with the rate e_1 over the unstable manifold; 2). The trajectory error of our algorithm has two stages, i.e. e_2 -rate at the beginning and e_1 later, which correspond exactly to two parts in our main theorem. 3). As $\lambda \to \infty$, the length of the first stage increases, meaning a smaller simulation error.

B.1. Training data of reaction-diffusion equation. We present the details of the training data preparation for the reaction-diffusion equation

(B.1)
$$\begin{split} \frac{\partial \mathbf{u}}{\partial t} &= D\Delta \mathbf{u} + \phi(\mathbf{u}), \quad T \in [0, 20], \\ \phi(\mathbf{u}) &= \phi(u, v) = \begin{pmatrix} u - u^3 - v + \alpha \\ \beta(u - v) \end{pmatrix}. \end{split}$$

where $\mathbf{u} = (u(x,y,t),v(x,y,t))^T \in \mathbb{R}^2$ are two interactive components, D is the diffusion matrix, and $\mathbf{R}(\mathbf{u})$ is source term for the reaction. The parameters are set to be $\alpha = 0.01, \beta = 1.0, D = \begin{pmatrix} \gamma & 0 \\ 0 & 2\gamma \end{pmatrix}, \gamma \in \{0.05, 0.10, 0.15, 0.20, 0.25\}$ in the simulation. To obtain the initial condition \mathbf{u}_0 , we first sample i.i.d. from a normal distribution:

(B.2)
$$u(x, y, 0), v(x, y, 0) \sim \mathcal{N}(0, 1).$$

Then, we solve the equation from this initial condition for 200 time steps with dt = 0.01 to obtain a physical velocity profile \mathbf{u} , which is taken to be the initial condition. The reason to discard the first 200 time step velocity profiles is that they appear to be less physical and we believe adding them into the training set will deteriorate the performance of the data-driven model. Lastly, the boundary condition is taken to be periodic in the simulation domain $[0,6.4]^2$. Given all this information, we solve the equation using the Crank-Nicolson scheme where the non-linear term is treated explicitly. The Δt of the simulation is set to 0.01 and a total time step 1000. To obtain the coarse-fine grid correction term, we first simulate the equation on the grid of size

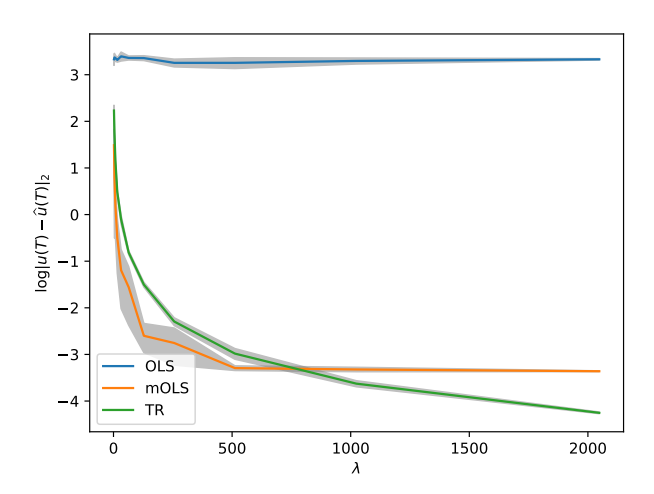


Fig. 7. In this figure, we compare our method with OLS and modified OLS. The horizontal axis denotes the strength of the penalty while the vertical axis denotes the accuracy of the prediction at terminal time. The scale of noise ϵ is set to 0.001, time steps to 50. All the cases have a low dimensional structure, i.e. only the first coordinate is non-zero. The shadow area represents the standard deviation calculated by 10 random tests. The first observation is that both regularized methods outperform the naive OLS method as regularization penalizes the deviation along the unstable direction. Secondly, the error of mOLS and TR both decrease as regularization becomes stronger. However, as λ becomes greater, the improvement of the mOLS algorithm ceases and cannot achieve better performance than 10^{-3} .

2n from initial condition \mathbf{u}_0^{2n} , which provides velocity profiles $\mathbf{u}_i^{2n}, i=0,1,2,\cdots,T$. Then, for each time step k, starting from the velocity profile \mathbf{u}_k^{2n} , we first restrict it via R_{2n}^n to obtain a velocity profile \mathbf{u}_k^n over grid n. Next, we iterate this profile one step by Crank-Nicolson scheme and interpolate it back to grid 2n via I_n^{2n} . The procedure is summarized as

(B.3)
$$\mathbf{y}_{k}^{2n} = \mathbf{u}_{k+1}^{2n} - I_{n}^{2n} \circ f_{n}(R_{2n}^{n}(\mathbf{u}_{k}^{2n})).$$

Along with $\mathbf{u}_k^{2n}, (\mathbf{u}_k^{2n}, \mathbf{y}_k^{2n})$ becomes a data pair we used to learn the unresolved model.

B.2. Training data of Navier-Stokes equation. We provide the details on the numerical scheme used to solve the Navier-Stokes equation with special focus on the resolved and unresolved parts of the solver. This is also the structure of our MLHS algorithm. This equation is written as follows

(B.4)
$$\frac{\partial \mathbf{u}}{\partial t} + (\mathbf{u} \cdot \nabla)\mathbf{u} - \nu \Delta \mathbf{u} = \nabla p, \quad T \in [0, 1],$$

$$\nabla \cdot \mathbf{u} = 0,$$

where $\mathbf{u} = (u(x,y,t),v(x,y,t))^T \in \mathbb{R}^2$ is velocity and p pressure.

The computational domain of the Navier-Stokes equation is $[0,4] \times [0,1]$ and we

use staggered grid pf size 128×32 and 256×64 . The boundary condition is given by

$$\begin{aligned} u\Big|_{y=0} &= v\Big|_{y=0} = u\Big|_{y=1} = v\Big|_{y=1} = 0, \\ p\Big|_{x=4} &= 0, \frac{\partial v}{\partial n}\Big|_{x=4} = 0, u\Big|_{x=0} = \exp\{-50(y-y_0)^2\}, \\ v\Big|_{x=0} &= \sin t \cdot \exp\{-50(y-y_0)^2\}. \end{aligned}$$

While the initial value of velocity u, v is set to vanish except for the boundary x = 0. To enforce the boundary condition, we use the ghost-cell method and the true computational boundary lies in the middle of the first grid cell. The grid size during the numerical simulation is given by $u:(n_x+2)\times(n_y+2), v:(n_x+2)\times(n_y+1), p:n_x\times n_y$ where $(n_x,n_y)=(128,32),(256,64)$. The pressure is obtained via solving a Poisson equation during each time step. Moreover, since the boundary ghost cells are only of numerical importance to force the boundary condition, we discard them when building the dataset of the Navier-Stokes simulation, i.e. the dataset consists of tuples $(u,v,p), u,v,p \in \mathbb{R}^{n_x\times n_y}$. Moreover, as we use staggered grid for simulation, the collocation points for u,v,p are different for all the grid cells. We linearly interpolate the value of u,v at the boundaries of cells to the middle point of cells which coincides with the collocation points for pressure to generate a consistent dataset. Similar to the reaction-diffusion case, we collect the field data after the first 100 iterations to avoid those unphysical fluid field configurations.

- **B.3.** Different distribution shift extents with different simulation parameters. For the Navier-Stokes equation, the degree of distribution shift is induced by varying the Reynolds number, which is verified in Figure 8. It shows that as the Reynolds number is increased, both the trajectory simulation error and distribution shift increase for almost all sampled time steps.
- **B.4.** Network model details. To capture the fluid patterns precisely, we use a modification of the U-net[46]. The main structure is an autoencoder whose encoder and decoder steps are constructed as convolutional blocks which serve as a non-linear dimension reduction. The skip connection is used between parallel layer to retain the information. The detailed architectures are described below where we only focus on one specific grid size.

We use the convolutional autoencoder to identify the intrinsic manifold of our training data. Specifically, the encoder is composed of a sequence of convolutional layers followed by max-pooling that extracts the information from a gradually large scale. The decoder is attached to the output of the encoder and is composed of a sequence of convolutional layers followed by upsampling to recover the state variable. For the depth of the encoder and decoder as well as the number of channels in each layer, we use the same setting as the network model for surrogate modeling discussed in the next paragraph. The key difference between the convolutional encoder we used for characterizing the underlying data manifold structure and the UNet for surrogate modeling is that UNet has skip connections between the layers of the same size in the encoder and decoder while the autoencoder does not. This is to avoid trivial reconstruction of the intrinsic manifold. For a more detailed discussion on using the convolutional autoencoder to approximate the nonlinear trial manifold, we recommend reading [28]. Regarding the training issue of the autoencoder, we use all the data (no train-test split). The depth and size of the bottleneck layer of the network need to be tuned to make sure the training loss is small enough. Our empirical observation is

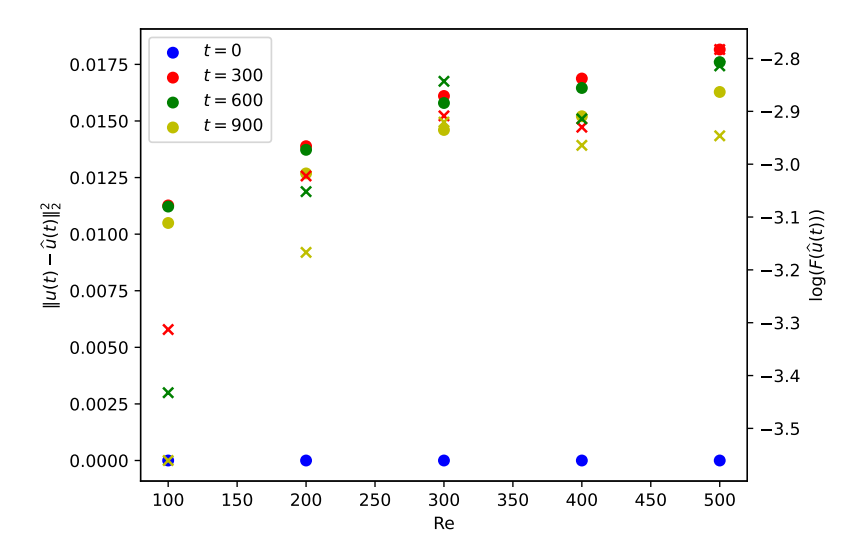


Fig. 8. In this figure, we illustrate the distribution shift and error of the simulated trajectories under different Reynolds numbers. The solid dots represent the error at given time steps and simulation parameter Re and the 'x's denote the log of the corresponding distribution shift calculated using autoencoder. Different time steps are distinguished using different colors. From the results, we conclude that as the Reynolds number increases, both the simulated error and distribution shift increase for almost all the sampled time steps. This verifies the intuition that the Navier-Stokes equation with a greater Reynolds number suffers from more severe distribution shift.

that if the optimization error of the autoencoder is not small enough, e.g. 10^{-1} , the performance of the regularized estimator will not show great improvement over the OLS estimator, meaning that the regularization is not effective. If the error is trained below 10^{-3} , then our algorithm has significant improvement over the benchmark and the performance is no longer sensitive to further decrease the training loss of the autoencoder.

For the reaction-diffusion equation, the domain is a square so we use square block with size 128, 64, 32, 16, 8, 4, 8, 16, 32, 64, 128 and number of blocks 2, 4, 8, 16, 16, 32, 16, 16, 8, 4, 2 respectively. In the downsampling stage where the block size shrinks to half each time, we use a convolutional layer with kernel size 4×4 , padding 1, and stride 2 followed by a batch normalization layer. In the upsampling stage, between each block where the size doubles, we first apply an upsampling layer with scale factor 2 followed by a convolutional layer with kernel size 3, padding 1, and stride 1 and again a batch-normalization layer. For the Navier-Stokes equation, the domain is a rectangle and the blocks are modified to adjust the height-width ratio. The block size follows $256 \times 64, 128 \times 32, 128 \times 32, 64 \times 16, 32 \times 8, 16 \times 4, 8 \times 2, 16 \times 4, 32 \times 8, 64 \times 16, 128 \times 32, 256 \times 64$ with the same block number at each level as reaction-diffusion cases. The only difference is that the output layer only contains one block since we are predicting the pressure, which only has one component.

During training different network models, we used Adam optimizer [24] with PyTorch [38] scheduling "ReduceLROnPlateau" and initial learning rate 10^{-4} . For each specific scenario, i.e. Navier-Stokes equation with Reynolds number 400 and grid size 128×32 , we generate 10 trajectories using high fidelity numerical solver. During training, one of them is randomly chosen as the test trajectory and others are used as training data. The training epoch of the autoencoder is set to 3000 and of the OLS and the TR estimator is set to 5000. The batch size is chosen to be 1000, which equals

the trajectory length. The constant K in $t_K = \arg \max_t \|\widehat{\mathbf{u}}_t - \mathbf{u}_t\| \le K$ is taken to be 100 during the experiment.

B.5. Choice of regularization strength. From a theoretical perspective, $\lambda \to \infty$ will provide the best estimator that stabilizes the hybrid simulation. However, as λ increases, it takes more time steps for the objective function to reach a fixed threshold. In practice, as we increase the value of λ while fixing the time steps, the final loss function keeps increasing and the estimator error, i.e. the former part of the loss function also increases. We compare four different choices of $\lambda = 1, 10, 100, 1000$ and fix it to 10 throughout the whole experiment.